Centre d'hydrogéologie et géothermie
Université de Neuchâtel

Master en hydrogéologie et géothermie
Spécialisation en hydrogéologie

Travail de fin d'étude

STOCHASTIC MODELING OF THE KARSTIC SYSTEM OF THE REGION OF TULUM (QUINTANA ROO, MEXICO)

Cécile VUILLEUMIER

Septembre 2011

Rue Emile-Argand 11
CH – 2000 Neuchâtel

Tél. ++41 32 718 26 02
Fax : ++41 32 718 26 03

Abstract

The region of Tulum (Quintana Roo, Mexico) is located on the east coast of the Yucatan Peninsula. It contains one of the most developed karst systems in the world, with some explored caves being more than 100 kilometers long. Because of the growing economic development, mainly in the field of tourism, the region has been attracting the attention of the environmental community in recent years. The urban development plan includes the construction of a 60,000-beds hotel complex (Supper et al., 2009), an airport and a motorway access (SCT, 2010). Moreover, in the Yucatan Peninsula, a small proportion of wastewater is treated before being reinjected into the aquifer (Marin et al., 2000). This suggests an important pollution risk in the area of Tulum, for the aquifer has a limited ability in contaminant retention or filtration resulting from its karstic nature. In addition, fragile ecosystems are threatened by the pollution of groundwater that feed them. These are a vast coral reef off the shore and the UNESCO Sian Ka'an Biosphere Reserve located a few kilometers south of Tulum.

To assess the vulnerability of the aquifer, this study presents the development of a numerical finite-element flow model. To account for the high heterogeneity of karst aquifers, various modeling techniques are available. The program Ground Water (Cornaton, 2007) allows the integration of 1D elements into mesh of the model. These ‘pipes’ are meant to stand for karstic conduits. To represent the duality of the flow that characterizes karst aquifers, flow in pipes is simulated in the turbulent regime.

Maps of explored caves are used to build the flow model. In addition, data from two airborne geophysical campaigns are available. These electromagnetic measurements allow the mapping of unexplored karstic conduits. The completion of the existing network map is achieved through the stochastic pseudo-genetic karst simulator developed by Borghi et al. (2011). This simulator allows the generation of a set of equiprobable realizations of the karst network. Geophysical data are employed to constrain the simulation.

The network is then integrated into the flow model. The calibration of the karstic network parameters (density, radius of the conduits) is conducted through a comparison with a set of GPS measurements of the piezometric level. Although the proposed models show great variability, they seem to reproduce realistically the heterogeneous flow of the aquifer. Simulated velocities in conduits are relatively fast, about 10 cm s^{-1}. The expected travel time between the city of Tulum and the sea are thus very short, suggesting a high risk of pollution of the coral reef by Tulum sewage.

Résumé

La région de Tulum (Quintana Roo, Mexique) se situe sur la côte est de la péninsule du Yucatan. Il s'y trouve un des systèmes karstiques les plus développés au monde, certaines grottes explorées mesurant plus de 100 kilomètres. En raison du développement économique grandissant, principalement dans le domaine du tourisme, la région attire l'attention des milieux écologiques depuis quelques années. Le plan de développement urbain inclut la construction d'un complexe hôtelier de 60'000 lits (Supper et al., 2009), d'un aéroport et d'un accès autoroutier (SCT, 2010). Par ailleurs, dans la péninsule du Yucatan, une faible proportion des eaux usées est traitée avant d'être réinjectée dans l'aquifère (Marin et al., 2000). La situation est préoccupante, notamment à cause de la nature karstique de l'aquifère, qui lui suggère une grande vulnérabilité. De plus, des écosystèmes fragiles sont menacés par la pollution des eaux qui les alimentent. Il s'agit d'un vaste récif corallien au large de la côte, ainsi que la réserve de Sian Ka'an, inscrite au patrimoine de l'UNESCO et située à quelques kilomètres au sud de Tulum.

Pour estimer la vulnérabilité de l'aquifère, cette étude présente le développement d'un modèle numérique à éléments finis simulant l'écoulement souterrain dans cette région. Pour rendre compte de la forte hétérogénéité caractérisant les aquifères karstiques, différentes techniques de modélisation existent. Le programme Ground Water (Cornaton, 2007) permet d'inclure des éléments 1D au maillage du modèle, soit des tuyaux représentant les conduits karstiques. Afin de représenter la dualité de l'écoulement régissant les aquifères karstiques, l'écoulement dans les tuyaux est simulé en régime turbulent.

Afin d'intégrer le réseau karstique au maillage du modèle, les cartes des grottes réalisées par des plongeurs ont été utilisées. Par ailleurs, des données résultant de deux campagnes de géophysique aéroportée dévoilent la présence de certains conduits inexplorés. Pour compléter le réseau existant, le simulateur pseudo-génétique de karst développé par Borghi et al. (2011) a été utilisé. Ce simulateur stochastique permet la génération d'un ensemble de réalisations équiprobables du réseau karstique. La modélisation est contrainte à l'aide des données géophysiques.

Le réseau est ensuite intégré au modèle d'écoulement. La calibration des paramètres du réseau karstique (densité, rayon des conduits) est réalisée au moyen d'une comparaison avec des mesures GPS du niveau piézométrique. Bien que les modèles proposés montrent une grande variabilité, ils semblent reproduire de manière réaliste l'écoulement très hétérogène de l'aquifère. Les vitesses simulées dans les conduits sont très rapides, de l'ordre de 10 cm s^{-1}. Les temps de trajet attendus entre la ville de Tulum et la mer sont donc très courts, ce qui suggère un grand risque de pollution du récif corallien par les eaux usées de Tulum.

Acknowledgments

I would like to express my heartfelt gratitude to Prof. Philippe Renard, first of all for introducing me to the enchanting topic of Yucatan karst as well as to the fascinating field of stochastic hydrogeology. I thank him also for giving me the opportunity of getting to Mexico and discover my study area, for his expert guidance, his infectious enthusiasm and for the plentiful of precious ideas and advices he provided in order to improve my work.

I am deeply indebted to Andrea Borghi, who spent a tremendous amount of time following my work and sharing with me his technical skills. He holds a great responsibility in the successful achievement of this thesis and for that I send him my sincerest appreciation.

This work was made possible thank to the collaboration of the Departement of Geophysics of the Geological Survey of Austria within the framework of the Xplore Project. I wish to thank especially Mag. Robert Supper, Mag. David Ottowitz and Dr. Arnulf Schiller for including me in their field team and for sharing with me their huge and high-quality database. Special thanks are addressed to David for his numerous advices and his proofreading.

I am very grateful to Prof. Fabien Cornaton, from the Centro del Agua para América Latina y el Caribe (Monterrey, Mexico), for giving me the chance of using his flow simulation code as well as for his advices on hydrogeological modelling. I express my gratitude also to Axa Maqueda for his nice and welcome help during the field work.

I wish to thank the Tulum cave divers Robbie Schmittner (Xibalba Dive Center) and Bil Phillips (Speleotech) for the most valuable assistance they provided during the field work. Only thanks to them we were able to access to most remote and wildest cenotes. Special thanks to Robbie for the information he shared with me.

Studying at the CHYN has been a wonderful experience for I have been surrounded by highly qualified and available researchers. I wish to thank especially Dr. Julien Straubhaar, Dr. Grégoire Mariethoz, Dr. Jaouher Kerrou and Damian Glenz for their valuable advices. On another hand, I wish to thank all my colleagues for the moments of laughter and of friendship we shared together. I think especially of Alexia, Cybèle, Damien, Jérémie and Lorienne (special thanks to her for her proofreading).

I cannot end without a word of thanks to my parents, for their support and the sincere interest they showed along my study years. I wish also to thank Maj for her unfailing, heart-warming and necessary friendship and Demian for his precious support and his love.

Table of contents

Abstract……I

Résumé……III

Acknowledgments……V

1. Introduction 1

2. Description of the study site 2

2.1 The Yucatan Peninsula aquifer 2

2.2 Settings of the karst network 4

3. Karst network modeling 5

3.1 Method 5

3.2 Processing the geophysical data 6

3.2.1 Method and data 6

3.2.2 Processing the data 7

3.2.3 Completing the electromagnetic map 10

3.3 Using the karst simulator 11

3.3.1 Building the velocity medium 11

3.3.2 Settings of the karst simulator 12

4. Hydrogeological modeling 16

4.1 Building the flow model 16

4.2 Sensitivity test of hydraulic parameters 17

4.3 Calibration of karst network parameters 18

5. Discussion 22

6. Conclusions 23

References 25

Appendix A : Measured electromagnetic response 27

Appendix B : Processed electromagnetic response 31

Appendix C : Water level measurements 35

1. Introduction

Figure 1 : Location of the study area (modified after Google Earth, 2011).

The Caribbean coast of the Yucatan Peninsula (Figure 1 and 2) is known to contain an important karst system which includes several of the longest underwater caves in the world (http://www.caverbob.com/uwcaves.htm, consulted on Sept. 12, 2011). It has been explored and mapped by cave divers since tens of years (Figure 3a). The aquifer consists in a fresh water lens of thickness between less than 10 to 100 meters on the top of a saline water intrusion reaching several tens of kilometers inland (Bauer-Gottwein et al., 2011). The relief is low and surface runoff is absent from the peninsula (Beddows, 2004). The karst system appears to be very well developed: the deepest explored cave lies at 119 meters depth (Smart et al., 2006) and the largest conduit diameters reach some seventy meters.

Because of the limited resource of the fresh water lens and the growing demand, water supply in the Yucatan Peninsula becomes problematic (Bauer-Gottwein et al., 2011). Especially in the area of Tulum (Quintana Roo, Mexico), environmental concerns are growing because of the planned urban development. It includes the buildings of a hotel complex (Supper et al., 2009), an airport and a highway (SCT, 2010). Moreover, it is common use in the Yucatan Peninsula to reinject wastewater into the aquifer without previous treatment (Marin et al., 2000). This pollution risk is a major threat for the nearby Sian Ka'an Biosphere Reserve and the large coral reef located near the shore (Figure 2). Indeed, they are host to ecosystems that are highly dependent on the karst aquifer (Gondwe, 2010) . To assess the vulnerability of the aquifer, a finite-element flow model has been built (Figure 3a). As the network geometry is a major constraint on flow paths and velocities in karstic aquifers (Worthington and Smart, 2003), it has to be incorporated in the model in order to provide realistic pollution scenarios.

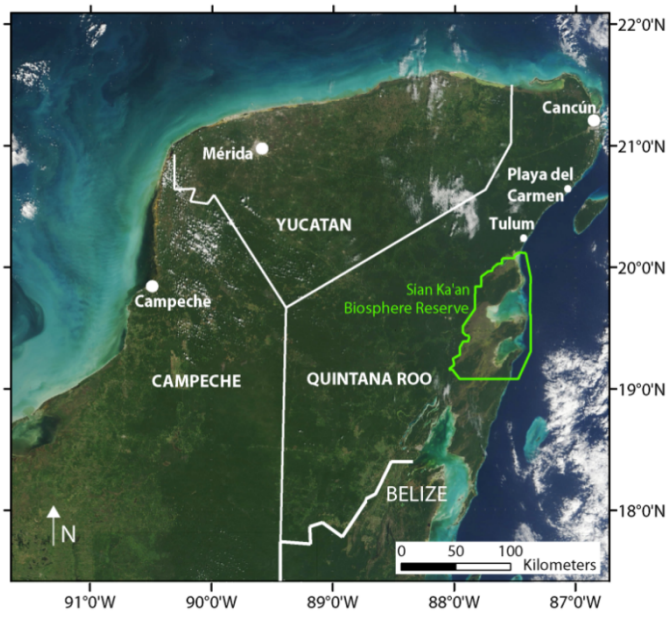

Figure 2 : Geographical situation of the Yucatan Peninsula. Modified after the NASA, http://rapidfire.sci.gsfc.nasa.gov/, Aug. 26, 2010.

Chapter 2 is a brief physical presentation of the study area. Chapter 3 focuses on the completion of the known karst network over the modeled area. For this purpose, airborne electromagnetic measurements realized by the Geological Survey of Austria (Figure 3b) were processed. Supper et

al. (2009) showed that this method is able to reveal the presence of underwater karstic conduits in this area thanks to the strong electric conductivity contrast between water-filled caves and the limestone matrix. This data was employed to constrain the generation of equiprobable karst network realizations using the stochastic karst simulator developed by Borghi et al. (2011). The hydrogeological modeling is described in Chapter 4. The generated karst networks are included in the flow model as 1D-pipes where flow is ruled by the Manning-Strickler formula rather than by Darcy's law, allowing the simulation of turbulent flow. Attempts to calibrate the model were made using high resolution GPS water level measurements (Figure 3b). Results are discussed in Chapter 5 and conclusions are presented in Chapter 6.

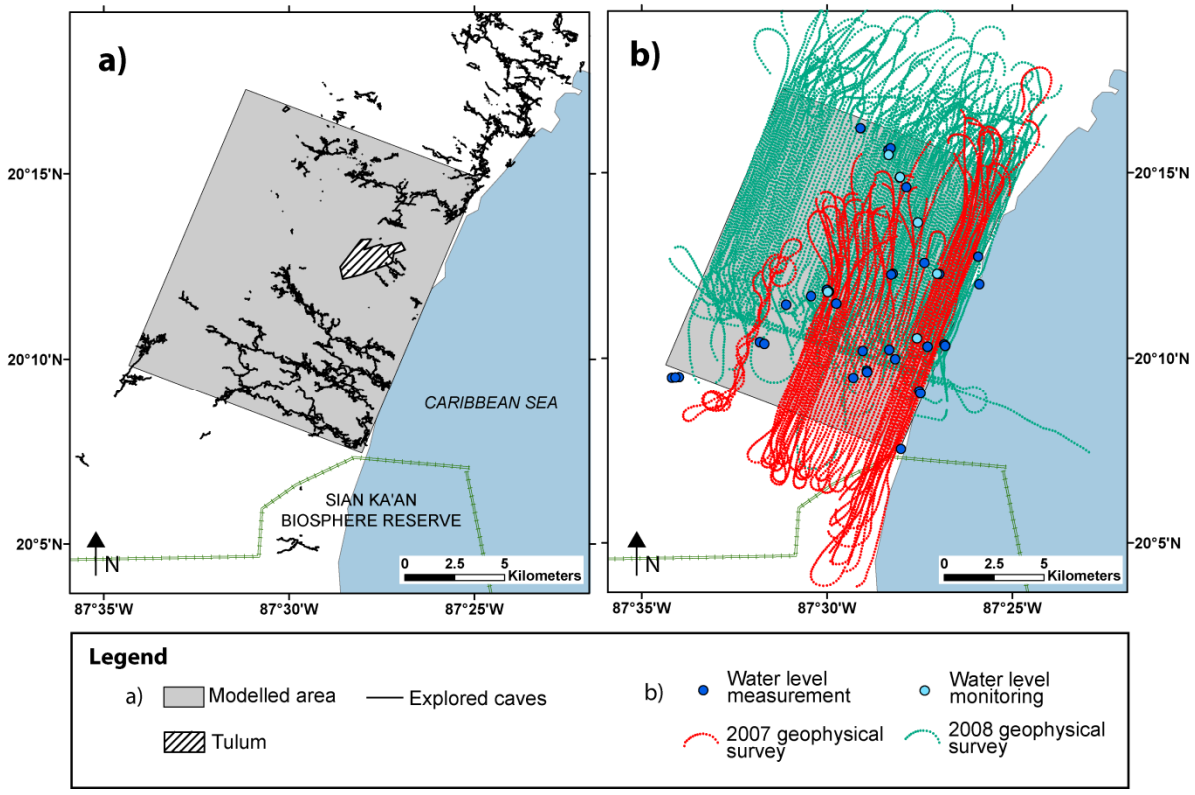

Figure 3 : Location of the modeled area and available data.

2. Description of the study site

2.1 The Yucatan Peninsula aquifer

The Yucatan Peninsula is a 300-kilometer wide carbonated platform located between the Gulf of Mexico and the Caribbean Sea (Figure 1 and 2). The overall topography is relatively low, maximum elevations reaching some 300 m.a.s.l. Mean annual temperature is 26° C and annual precipitations are between 1000 and 1400 mm y^{-1}, the major part falling during the wet season from May to October (Héraud-Piña, 1996). Surface runoff is absent (Beddows, 2004) and, according to Gondwe et al. (2010), the estimated recharge for the south-eastern peninsula is 17% of the precipitation.

The aquifer is densely stratified and consists in a cooler fresh water lens on top of a warmer saline water intrusion (Beddows et al., 2007). General groundwater circulation is organized in a concentric flow from the center of the peninsula towards the coast. Regional hydraulic gradient is relatively low, estimates lying between 1 to 10 cm km^{-1} for coastal plains (Bauer-Gottwein et al., 2011).

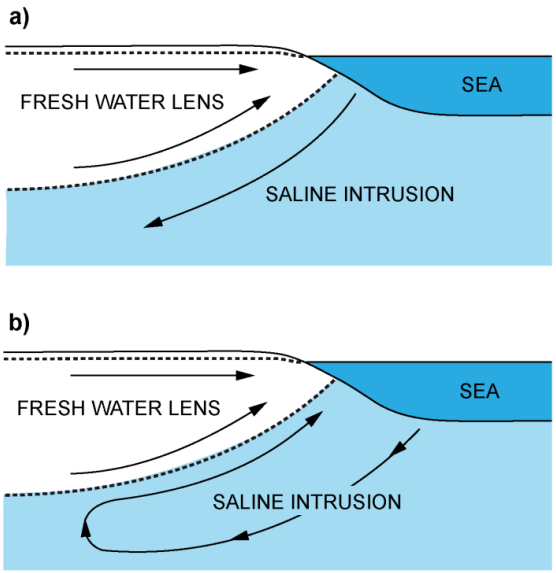

Figure 4 : Two conceptual models of deep water circulation in the eastern Yucatan peninsula, as proposed by Beddows et al. (2007) in a) and Stoessel et al. (2002) in b).

The groundwater hydrodynamics is characteristic of heavily karstified aquifers. According to the review of Bauer-Gottwein et al. (2011), estimations of the hydraulic conductivity of Yucatan Peninsula aquifer vary extensively depending on the scale of interest. Testing of core samples gives values of 10^{-6} to $5 \cdot 10^{-2}$ m s^{-1} while calibration of flow models at scale of hundreds of kilometers yield values in the range 10^{-1} to 10^{2} m s^{-1}. As for groundwater velocity, Moore et al. (1992) measured values in fractures increasing coastward from 1 to 12 cm s^{-1}. In the limestone matrix, they obtain values in the range of 10^{-2} cm s^{-1}. Beddows (2004) provides measurements for two conduits that were monitored for several months. These data reveal an important and rapid effect of sea level variations on the conduit flow velocity. Most of recorded values are in the range of a few centimeters per second, with a maximum of ~20 cm s^{-1} at a coastal site. Cave diver indications that flow is sometimes too strong to swim against suggests that velocities can reach several tens of centimeters per second.

The fresh water lens constituting the Yucatan Peninsula aquifer is relatively thin: its maximum thickness is approximately 100 meters (Bauer-Gottwein et al., 2011). The depth of the interface between the fresh water lens and the saline intrusion increases inland following a linear trend rather than the Dupuit-Ghyben-Herzberg model, possibly because of the influence of the karstic network (Beddows, 2004). In southern Quintana Roo, the fresh water lens discharges to the sea at a rate of 0.27 m^3 s^{-1} to 0.73 m^3 s^{-1} per km of coastline, depending on estimations (Bauer-Gottwein et al., 2011). Beddows et al. (2007) suggest that the saline water right underneath the fresh water lens flows in an opposite direction, contrary to the conventional model of densely stratified coastal aquifers proposed by Copper (1959) (Figure 4a). They base their hypothesis on numerous water temperature and electric conductivity measurements in *cenotes* (local name for sinkholes) and conduits. It is also corroborated by their observation of a very sharp, reflective halocline in some conduits, which could results from the decoupled circulation of fresh and saline waters. However, some authors disagree with this flow model. Stoessel et al. (2002) propose that the saline water zone flow is driven by geothermal convection cells (Figure 4b). The study of temperature profiles in three cenotes in the vicinity of Playa del Carmen (Quintana Roo) revealed the presence of positive thermal anomalies localized just below the mixing zone. According to their conceptual model, sea water enters the aquifer at a few hundred meters depth and is heated up by geothermal heat while flowing inland. It then rises up by buoyancy and is stopped by the mixing with the cooler fresh water. The coastward flow of this warm sea water might thus explain the thermal anomalies observed in cenotes. Thomas (2010) suggests that

convection cells are also present in the fresh water lens, and might play a role in the formation of vertical conduits and cenotes.

2.2 Settings of the karst network

The Yucatan Peninsula consists in a pile of Mesozoic and Cenozoic sediments on top of a Paleozoic basement. According to seven drillings realized in the northern peninsula at depth between 1.5 to 3.5 km, there is no low-solubility geological formation that could constrain the formation of karst at large scale (Ward et al., 1995). The upper hundreds of meters are sub-horizontally oriented limestones and dolomites (SGM, 2007) that show a high solubility (Marin et al., 2000). These carbonates are indeed very karstified, containing one of the most developed cave system in the world. Karstification may have been proceeding since late Eocene, when the peninsula emerged (Iturralde-Vinent and MacPhee, 1999).

Smart et al. (2006) presented a study of conduit geometry and distribution on the Caribbean coast of the peninsula, as well as assumptions about the processes ruling cave development in this area. According to them, the Yucatan cave system represents an intermediate type between telogenetic and eogenitic karst, following the classification proposed by Vacher and Mylroie (2002). The first type includes typical continental karst, where speleogenesis proceeds under the influence of water flowing from infiltration points toward base level. Cave development is mainly influenced by recharge and secondary porosity, which creates preferential flow paths. On the opposite, eogenetic karst development, also known as flank-margin model, is typical of small carbonated islands. In this case, speleogenesis occurs in diagenetically immature sediments presenting a high primary porosity. Mixing corrosion at the interface between fresh and saline water is the major process ruling carbonate dissolution. The resulting karst system consists in isolated chambers developing along the coast.

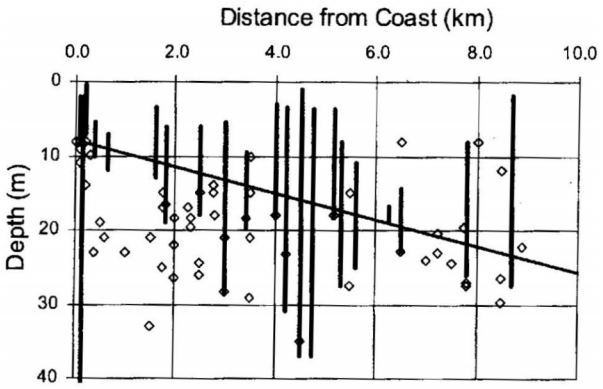

Figure 6 : Cave depths (vertical bars: depth range of one cave, diamonds: maximum depth) and halocline linear trend versus distance from the coast. Smart et al., 2006.

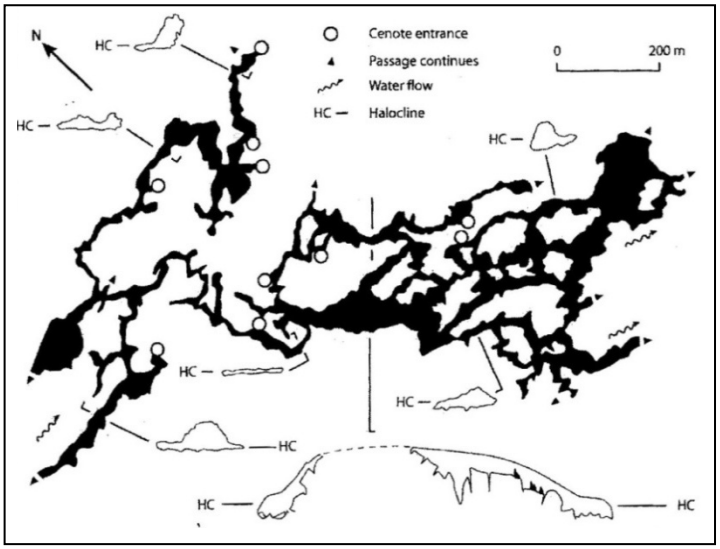

Figure 5 : Plan and passage cross sections with relative halocline position of Balam Can Chee cave, Nohoch Nah Chich system, Tulum. Passage cross sections are four times plan scale. Smart et al., 2006.

Following the observations of Smart et al. (2006), mixing corrosion has a major influence on the development of the Quintana Roo caves. Their study of conduit depths shows a correlation with the halocline position (Figure 6). Many of the conduit cross sections are enlarged at the fresh – saline water interface (Figure 5), which is in some locations very sharp (Beddows et al., 2007). Caves located above or below the interface often show speleothems or recristallisation features that suggest that dissolution is not active there anymore. Moreover, the authors were able to link these paleo-karst horizons to previous sea level low or high stands. However, the flank-margin model cannot account on its own for the wide extend of the Yucatan karst system. Caves are organized into large anastomosing systems discharging to the sea, extending up to 8 - 12 kilometers inland (Figure 3a). This morphology suggests, on one hand, the action of an important discharge toward the sea in the process of cave development, on another, the lack of preferential orientation in conduit directions suggests their development in a high porosity matrix rather than in a heterogeneous fractured matrix.

3. Karst network modeling

3.1 Method

The karst modeling was achieved through the Borghi et al. (2011) stochastic pseudo-genetic karst simulator. The main input of the simulator is a velocity field that reflects the ability of the medium to get karstified. It is thus a representation of similar preferential flow paths for karstic conduits in a specific environment. For typical continental karst systems, this field is built by means of a geological model with higher velocities assigned to soluble formations, faults and/or fractures. Other input parameters are the inlet and outlet points of the network. Inlet points are typically sinkholes or dolines while outlet points are springs. They can be positioned either deterministically or stochastically. If the precise location of springs is unknown, it is possible to select a diffuse spring zone. In this case, the algorithm selects most probable outlet points in the given area. The last main parameter to set is the number of iterations and the number of generated conduits per iteration.

By means of a fast-marching algorithm, the velocity field is converted to a travel-time map between any locations of the domain and the springs(s). Assuming that the water follows the minimum effort path, conduits are generated along the shortest path from each inlet to the spring(s). For the following iterations, simulated conduits are considered as very high velocity path, inducing the generation of a hierarchized network.

The observations presented in Chapter 2.2 lead to a conceptual model of the system where caves develop mainly on a sub-horizontal plane toward the sea with no or little geological constraint. Thus, the conditioning of the karst simulation cannot be successfully achieved by means of a geological model. However, as mentioned in Chapter 1, the area has been extensively explored by two airborne geophysical campaigns. Supper et al. (2009) and Ottowitz (2009) already mentioned the ability of theses electromagnetic measurements to reveal karstic conduits. We thus present in this study a new use of the pseudo-genetic karst simulator, using the electromagnetic map for building the velocity field.

3.2 Processing the geophysical data

3.2.1 Method and data

The airborne geophysical measurements were carried out by the Geological Survey of Austria during two campaigns in 2007 and 2008. They cover an area of approximately 140 km^2 around the town of Tulum and are distributed along flight paths oriented N22 with a spacing of 20 to 100 meters (Figure 3b). They were obtained by means of an active frequency-domain electromagnetic method. In principle, the generated primary field induces eddy currents in the subsurface, which themselves creates a secondary magnetic field. The amplitude and phase of the secondary field depends on the electrical resistivity of the subsurface. Thanks to a strong contrast in resistivity between water-filled conduits and the surrounding limestone matrix, anomalous responses are expected were conduits are located. This method is thought to be particularly efficient in Tulum area, because of a very flat topography, a thin soil cover and the relatively shallow position of the main karst features (Supper et al., 2009).

The main part of the measurement system consists of a modified GEOTECH-"Bird" of 5.6 m length and 140 kg weight (Motschka, 2001). It is towed on a cable 30 m below the helicopter and transmitter coils inside the probe generate primary electromagnetic fields of four frequencies (340 Hz, 3200 Hz, 7190 Hz and 28850 Hz). The resultant secondary field is recorded by the corresponding receiver coils. For every frequency there are two measurement values, the in-phase (no phase shift between primary and secondary field) and the out-phase component (90° phase shift). Results are given in part per

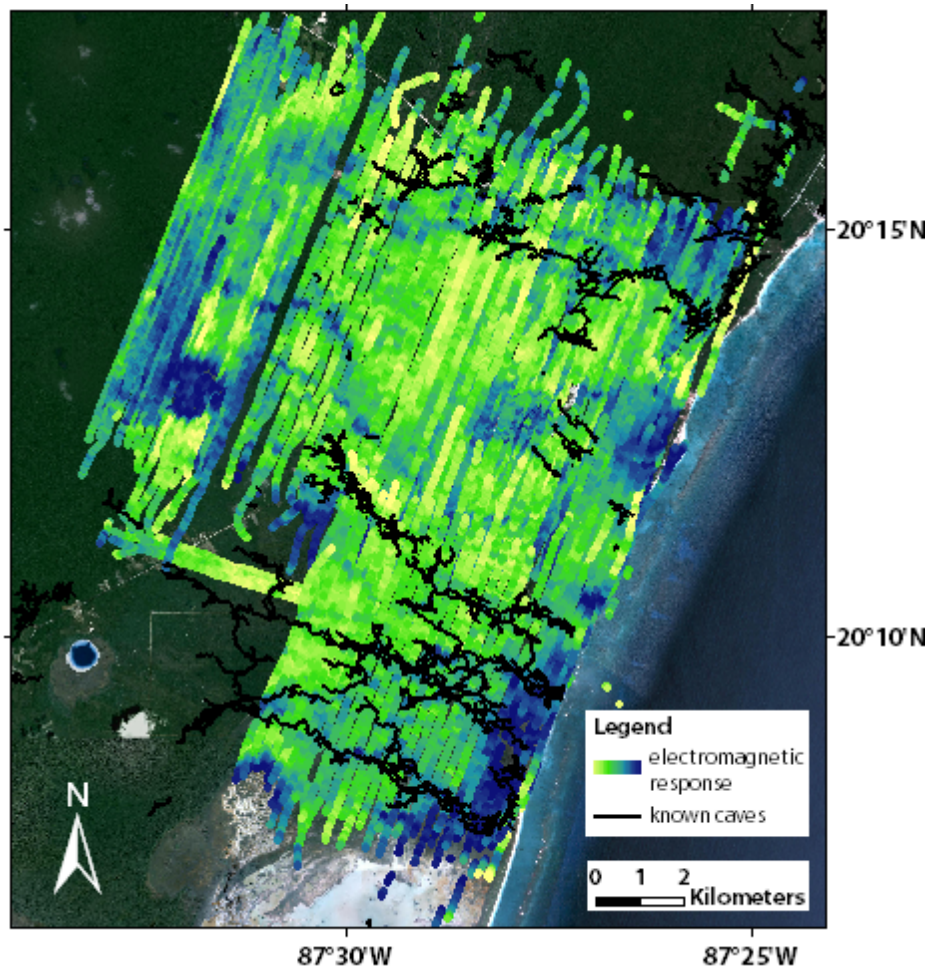

Figure 7: Measured amplitude (after altitude correction) of the field induced by a frequency of 7190 Hz. In the northern area (2008 survey, see Figure 3b), the measured out-phase component is shown and the southern area (2007 survey) it is the in-phase component. These data sets were chosen by comparing them with the known cave system. Indeed, a positive anomaly is observable around some known conduits. Color scale is histogram equalized, ranging from 2 to 20 ppm for the northern area and from 14 to 57 ppm for the southern.

million, being the ratio of the secondary field amplitude over the primary field amplitude. The data that gives best insight on the karstic conduits are the in-phase (north) and out-phase (south) component of the measured signal for a primary alternating field of the third frequency (7190 Hz). They were chosen on the basis of a visual analysis. Indeed, a comparison with the map of explored conduits (Figure 7 and Appendix A) shows a good agreement between conduits and anomalous electromagnetic response: anomalies are measured around known conduits. On another hand, the electromagnetic map reveals potential unexplored conduits.

However, variation of the signal amplitude can be induced by many factors. It is influenced by groundwater salinity, which varies across the study area. Thus, a global rise in conductivity toward the coast is observed, linked with the shallower depth of the halocline. Other identified sources of noises are a circular lagoon west of Tulum, the town of Tulum itself, and a drift between the flight paths (Figure 7). In addition, the sharpness of conduit-induced anomaly highly depends on the conduit size, depth and on the resistivity contrast between the water filling the conduit and the surrounding matrix. For some of these reasons and a few others, which are beyond the scope of this thesis, available electromagnetic inversion techniques do not yield a satisfactory efficiency in the mapping of karstic conduits. Instead, the selection of potentially conduit-induced anomalies was realized directly through the processing of the electromagnetic response (ppm values). This is described in paragraph 3.2.2.

3.2.2 Processing the data

A first step, realized by the Geological Survey of Austria, was taken by applying a 1) an altitude correction (method from Huang, 2008) and 2) a median filter. The correction is efficient in reducing the influence of altitude variation of the bird. The median filter, on the other hand, enhances conduit-induced anomalies. Figure 8 shows the histograms of the common logarithm of both data sets after correction and filter. Because of their logarithmic distribution, the common logarithm of both variables was used for the further processing. Their spatial distribution is shown in Figure 9a. With one another, they can be described as $E_m(\vec{x}_i)$, i.e. the value of the electromagnetic signal at each measurement point. This variable is unsuitable for the karst simulator for two reasons: a) some extremely high positive values do not seem to be linked with a resistivity anomaly (map in Figure 9a); b) the two data sets have slightly different distributions (Figure 8), which may produce artifacts in the conduit generation.

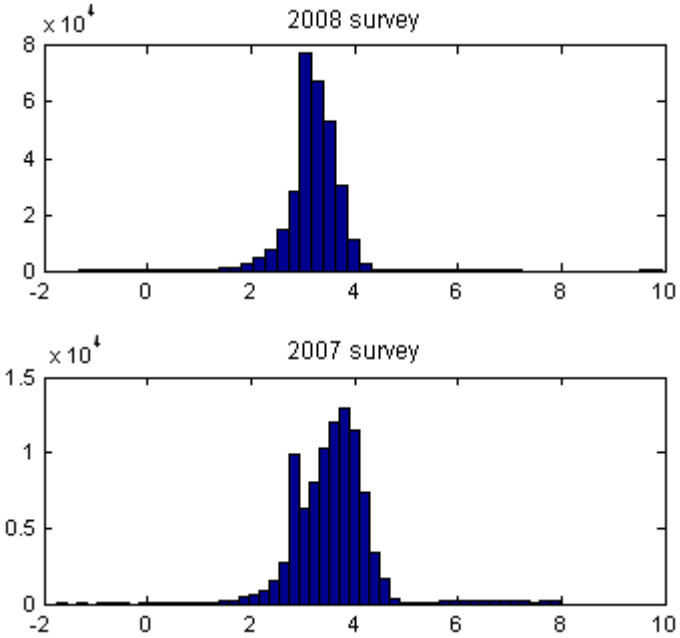

Figure 8 : Histograms of the common logarithm values of electromagnetic signal of both surveys after the median filter.

To cope with extreme values, those ranging beyond the interval of three standard deviations from the mean value were considered as outliers and removed. Resulting data fields are depicted in Figure 9b. To obtain a homogenous range, a normal score transform was applied to both variables, resulting in the new variable $N_m(\vec{x}_i)$, the normalized electromagnetic signal. This transformation reclassifies

values so that they follow a normal distribution with a mean value of 0 and a standard deviation of 1. At first, the values of the considered variable *w* are sorted in ascending order. The cumulative distribution function *F* of the variable is then computed. For each value E_m^i taken by the variable *w*, *F* gives the probability that *w* is less than E_m^i :

$$\boldsymbol{F\left(E_m^i\right) = P(w < E_m^i)} \quad \textbf{(1)}$$

Given *G*, the cumulative standard normal distribution, each value E_m^i is replaced by the *X* value of *G* at $P = F(E_m^i)$:

$$\boldsymbol{N_m^i = G^{-1}(F\left(E_m^i\right))} \quad \textbf{(2)}$$

The data field resulting from the normal score transform is illustrated in Figure 9c.

Using the software Isatis (v10.03, Geovariances, 2011), the resulting variable $N_m(\vec{x}_i)$ was interpolated to $N_m(\vec{x})$ with the kriging method on a regular grid of 20 by 20 meter cells. The origin of the grid (southern vertex) is positioned at (451100; 2225280) in the UTM Zone 16N coordinate system (datum WGS84). Its dimensions are 11.8 by 14.8 kilometers and its orientation N22 (Figure 3). First, the experimental variogram of the variable was computed for twenty distance lags of 20 meters each. After curve fitting, the chosen variogram model used for the interpolation is an exponential variogram with a range of 70 meters and a sill of 0.95. Some residual flight path noise still appears on the interpolated data field. To reduce it, a moving average filter for a window of 100 by 20 meters was applied, the longer axis of the ellipsoid being oriented perpendicular to the flight paths (i.e. N68). The final normalized electromagnetic signal $\widetilde{N}_m(\vec{x})$ is shown in Figure 9d and in Appendix B.

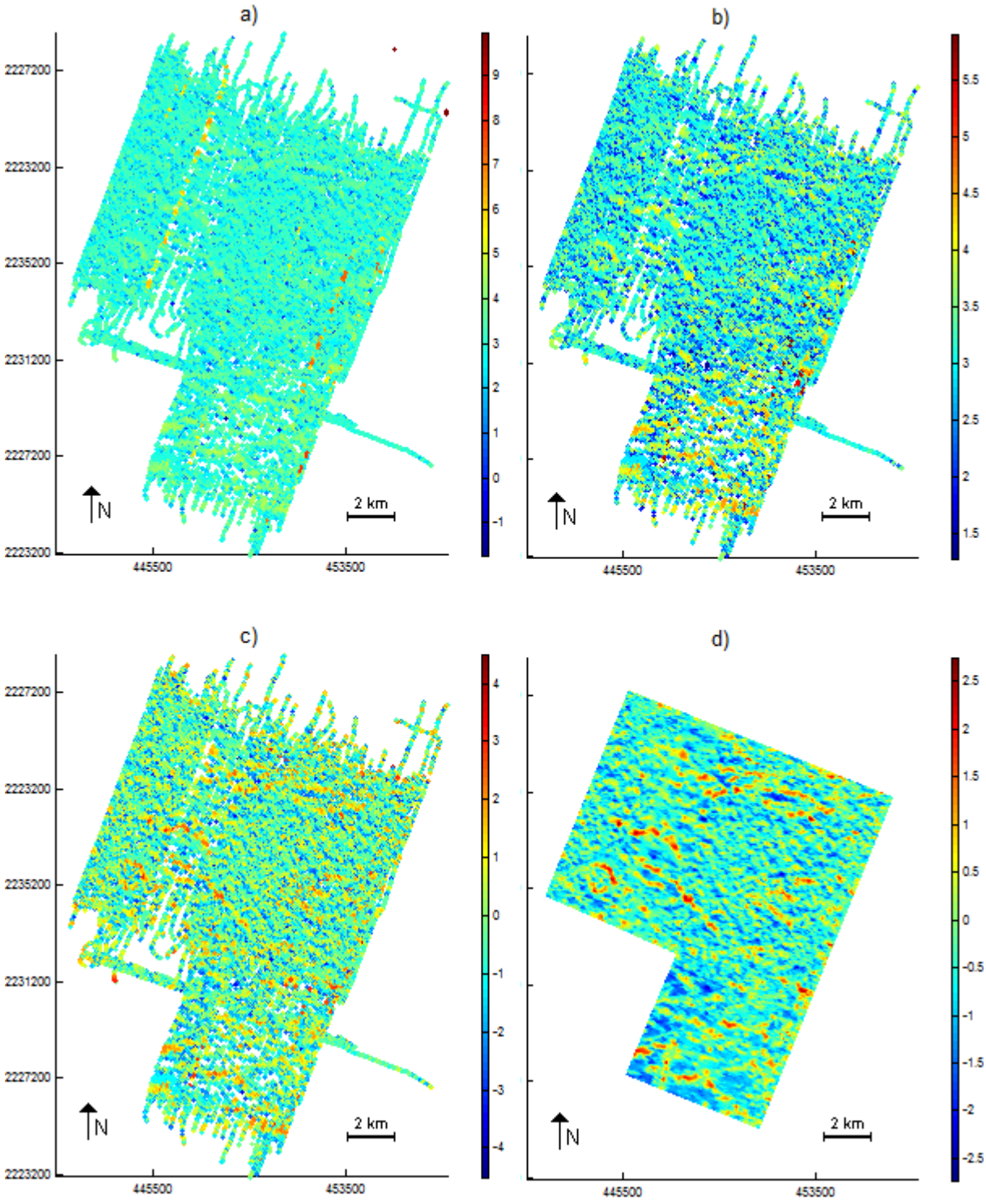

Figure 9 : a) Common logarithm of the magnitude of the out-phase (North) and in-phase (South) component of 7190 Hz after altitude correction and median filter; b) after removal of extreme values; c) after normal score transform on both data fields; d) after kriging and moving average. Coordinate system is UTM Zone 16N, WGS84.

3.2.3 Completing the electromagnetic map

A final step in the processing of the geophysical data was taken by completing the south-western part of the electromagnetic map. Indeed, this zone has not been surveyed by geophysical measurements. However, available cave maps indicate that major conduits are located in this area (Figure 3). The anomalous signal caused by a lagoon north-west of Tulum was also replaced by a simulated signal. This was achieved using the direct sampling, a multiple point geostatistical method developed by Mariethoz et al. (2010). In principle, the algorithm works by comparing available data with a so-called training image – in the present case, a portion of the data itself (direct sampling). For each point to simulate, the simulator scans the training image looking for a point that has a similar neighborhood. When it finds a point whose surrounding values are close enough (depending on the search window and the 'distance' threshold set by the user, i.e. the cumulated difference between each pair of neighboring points), its value is copied to the simulation grid.

The simulation grid is the same as defined in paragraph 3.2.2. The available cave map allows the realization of a bivariate simulation, variable 1 being the modified geophysical signal and variable 2 the presence of conduits (categorical variable, 1=conduit is present; 0=conduit is absent). Doing so, the simulation of the geophysical signal is made taking into account its relation with the presence of caves. However, simulated conduit maps are not used further in the study, because this technique fails to reproduce karstic system patterns – conduits are not connected to each other. The area of the Ox Bel Ha system was chosen as a training image, for it has been extensively surveyed by cave divers and by the 2007 geophysical campaign (Figure 3b). It was inferred that, in this zone, all the caves were known, i.e. the conduits are considered as absent where no information is provided. The conditioning data consists of, for variable 1, the whole geophysical data (Figure 10a). Variable 2 is built with the cave map: it is equal to 1 where a known cave is located. The rest of the map is set as being not informed (Figure 10b). The search radius is set to 50 meters and the distance threshold to 0.01. Twice as much weight is given to variable 1 as to variable 2 for the distance calculation. One realization is illustrated in Figure 10c, and the mean simulated signal for 100 equiprobable realizations is shown in Figure 10d. A positive anomaly is calculated around known conduits, while the remaining of the map shows strong variability, reflecting the uncertainty on the data in this area.

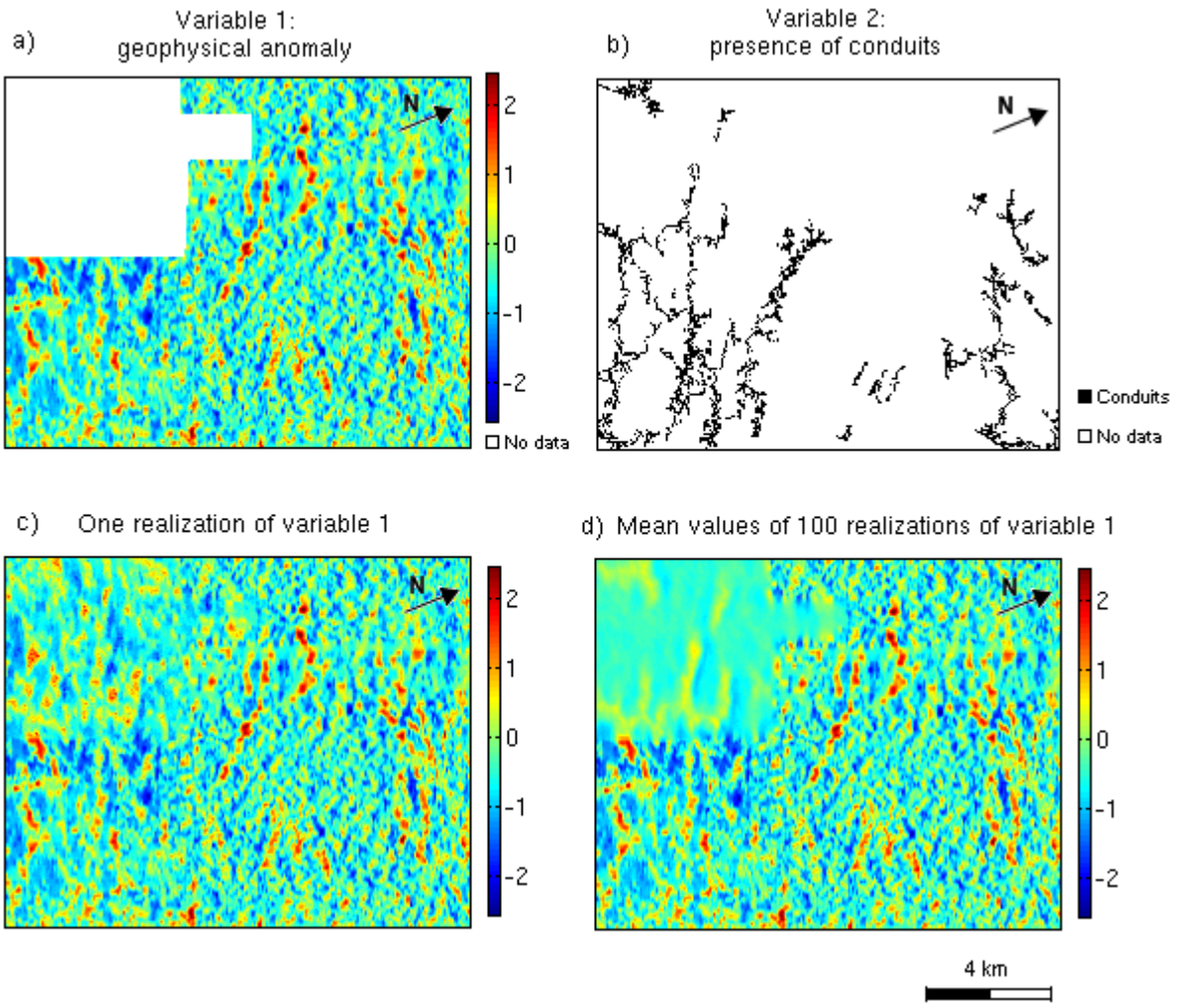

Figure 10 : a) and b) show the conditioning data for the extrapolation with direct sampling. The training image is the lower-left quarter of the simulation grid. c) is one random realization of the geophysical anomaly and d) mean values of 100 realizations.

3.3 Using the karst simulator

3.3.1 Building the velocity medium

Two pieces of information are used to create a velocity medium for the karst simulator: the modified electromagnetic map and the cave map. As for the electromagnetic map, considering that the simulator does not support negative values, velocities were uniformly shifted to be greater than zero by adding the minimum value taken by $\tilde{N}_m(\vec{x})$ to every point: $\dot{N}_m(\vec{x}) = \tilde{N}_m(\vec{x}) + \tilde{N}_m^0$. The 'cave' component is a Boolean variable constructed by the projection of the cave maps on the simulation grid. It is equal to 1 where cave are present and 0 where no information is provided. It can thus be described by an indicator function:

$$I_c(\vec{x}) = \begin{cases} \mathbf{1}\ \boldsymbol{if\ a\ cave\ is\ present\ at}\ \vec{\boldsymbol{x}} \\ \mathbf{0}\ \boldsymbol{otherwise} \end{cases} \quad (3)$$

A high velocity K_c, being the maximum value of taken by $\dot{N}_m(\vec{x})$, is assigned to points where $I_c(\vec{x}) = 1$. A first trial on a small portion of the simulation area is shown in Figure 11a. It appears that the

velocity contrast has to be strengthen for a proper control of the electromagnetic map on the karst simulation. It is realized using the assignment $K = b^{\dot{N}_m(\vec{x})}$. After some trial and error, the value of 3 for b is chosen as it provides a good constrain to conduit generation (Figure 11b). The velocity medium K as defined by Borghi et al. (2011) can thus be described as:

$$\boldsymbol{K(\vec{x}) = I_c(\vec{x}) \cdot K_c + [1 - I_c(\vec{x})] \cdot 3^{\dot{N}_m(\vec{x})}} \quad \textbf{(4)}$$

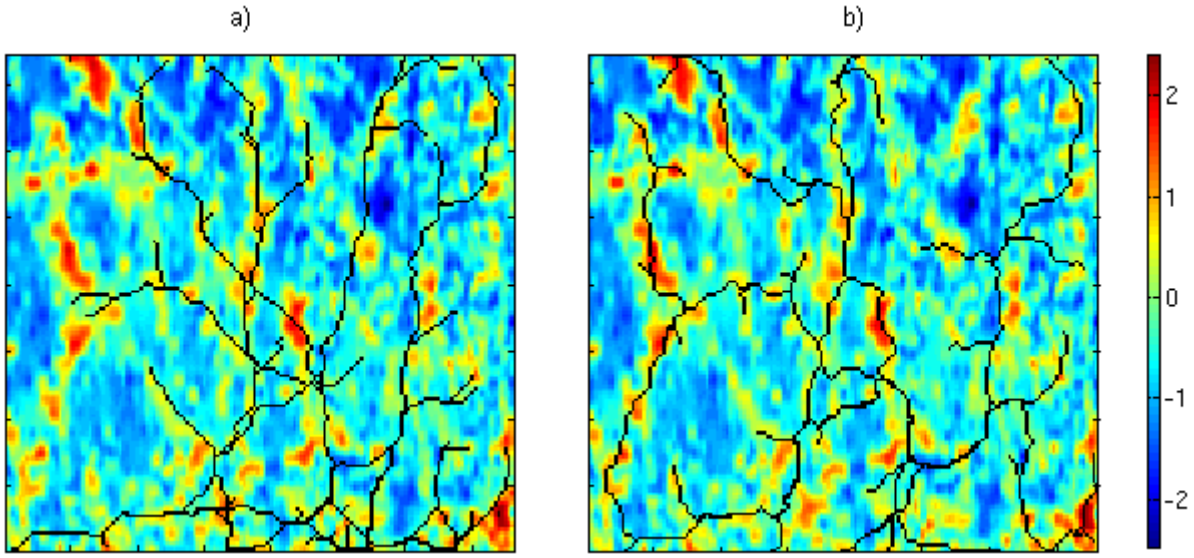

Figure 11 : Two karst simulation attempts on a small portion of the simulation area. In a), the electromagnetic component of the velocity medium is the electromagnetic map with positively shifted values (spatial variable *e*). In b), the electromagnetic control on the karst simulation is enhanced by setting its value to 3^e. In both cases, a diffuse spring zone is set at the lower border of the model. Conduit starting points are picked randomly on the map.

3.3.2 Settings of the karst simulator

Next step is the determination of in- and outlet points of the simulated karst system. Little information about the conduit inlets is available, the numerous cenotes present on the surface being not consistently linked with the underground network (Beddows, 2004). They are thus picked randomly for each conduit simulation in high velocity zones – i.e. where the presence of a conduit is suggested by cave exploration or a geophysical anomaly. The chosen threshold value for the inlet points is the third quartile of the velocity values, so that a quarter of the grid points can be potentially picked as a conduit inlet. An additional constrain is applied to for determination of the starting points of the first iteration: they must be located on the upper border of the model. This is done in order to ease flow simulation, a water inflow being located at this specific border (Chapter 4).

As for the outlets of the system, it has been established in Chapter 2 that the aquifer discharges to the sea. Without more precise information on the location of submarine springs, the option of a diffuse spring zone located on the coast was chosen. Two attempts for the configuration of the spring zone were made: 1) all the coast is selected as a spring zone; 2) alternation between both halves of the coast at each iteration. This latest option is expected to increase reconnections between the conduits, in order to reproduce the anastomosed patterns that are observed.

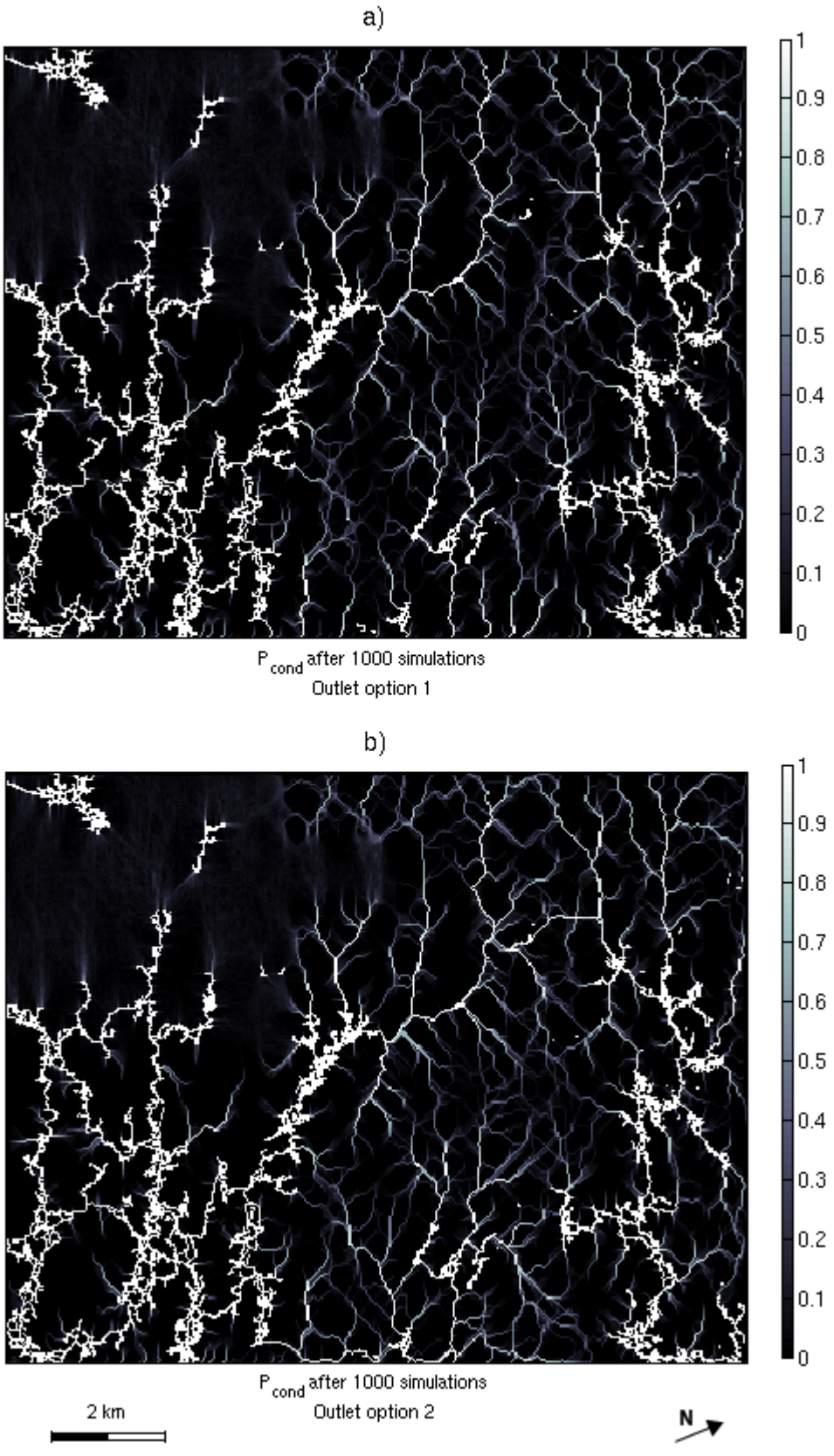

Figure 12 : Conduit occurrence probability map computed on the basis of 1000 realizations. In a), a diffuse spring zone is defined along the coast (low border of the simulation grid). In b), the spring zone is split in two. Each half of the coast is possible conduit outlet, alternatively between each iteration. Three iteration are computed, with respectively 20, 100 and 1000 generated conduits.

Figure 12 illustrates the conduit occurrence probability after 1000 realizations for both spring zone options. Simulation grid has the same extent as previously defined, but it is discretized in 40 by 40 meters squares. Three iterations are computed, with respectively 20, 100 and 1000 generated conduits per iteration. It appears that the built velocity medium is a good constrain to the simulation, as some conduits have an occurrence probability of over 0.8. As expected, network branches are more connected with an alternating spring zone (Figure 12b). Also, conduit orientations show much variability. With a uniform outlet area, conduits are mainly oriented straightly coastward and are organized in dendritic patterns (Figure 12a). Conduit distribution simulated with the second option is thus in better agreement with field observations. Furthermore, it can be observed in that conduit paths have a wider variability with option 2 (Figure 12b). With option 1, most probable conduits ($P > 0.8$) are mainly located on the same paths (Figure 12a). It is another argument to prefer option 2, as it reflects the high uncertainty arising from this cave mapping method. Following simulations presented in this work are thus realized with an alternating spring zone.

The remaining input parameters to set are the number of iterations and the number of conduits generated at each iteration. The hierarchization of the conduits directly arises from the number of computed iterations: when a conduit is simulated on the same path than a conduit resulting from a previous iteration, its order increases by one unit. This is illustrated in Figure 13. The maximum order is thus the total number of iterations. As a matter of simplification, the network is hierarchized in three orders; thus three iterations are computed. The known network is then included in the model. If no conduit was simulated on a known conduit, its order is 1. Otherwise, the ordering given by the simulation output is kept.

The number of generated conduits determines the overall density of the network. As this parameter in unknown, three network densities were generated and tested in the flow model (Chapter 4). Their parameters are described in Table 1 and they are illustrated in Figure 14.

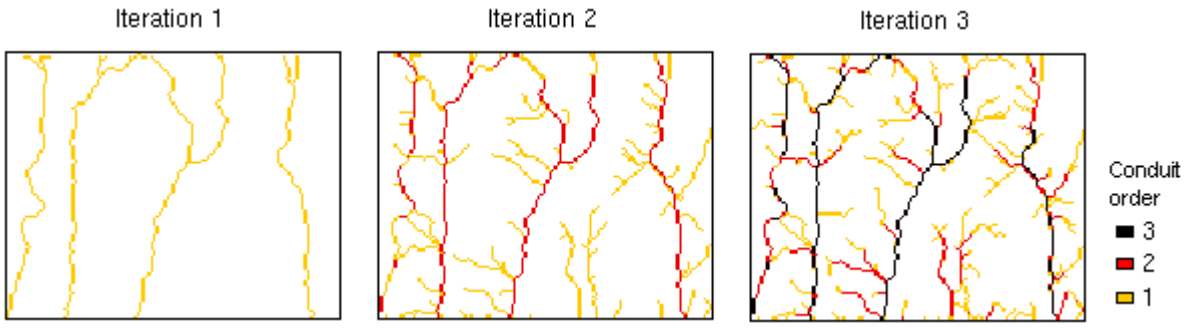

Figure 13 : Simulation of a three-iteration network. Each time a conduit is simulated on the same path as a conduit generated in a previous iteration, its order increases by one unit.

Table 1 : Input parameters of the three simulated networks.

Number of generated conduits	**Iteration 1**	**Iteration 2**	**Iteration 3**
Network 1	20	100	1000
Network 2	20	100	1500
Network 3	20	100	2000

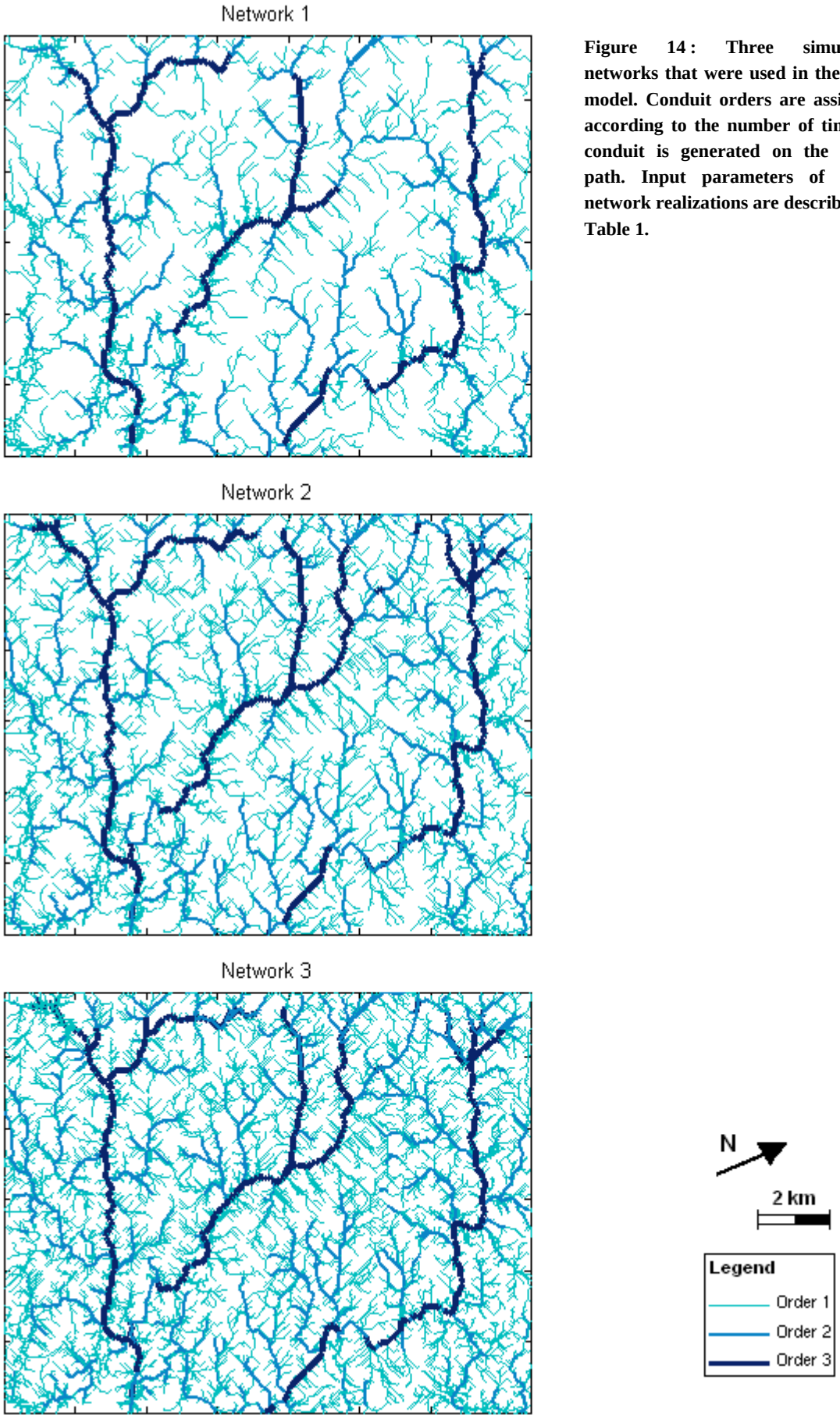

Figure 14 : Three simulated networks that were used in the flow model. Conduit orders are assigned according to the number of times a conduit is generated on the same path. Input parameters of these network realizations are described in Table 1.

4. Hydrogeological modeling

4.1 Building the flow model

The hydrogeological modeling was achieved using the finite-element flow model software Ground Water (Cornaton, 2007). For the purpose of this study, the built model is restricted to the fresh water lens which is represented as a 2D confined aquifer of constant thickness. The model is discretized in 40 by 40 meters squares (4-nodes elements) and the simulated karstic network is integrated in the mesh as a set of 1D elements (2-nodes elements) (Figure 15). Small network branches that are not linked with any outlet (results of cave exploration) are removed before each flow simulation, so that the computation reaches convergence.

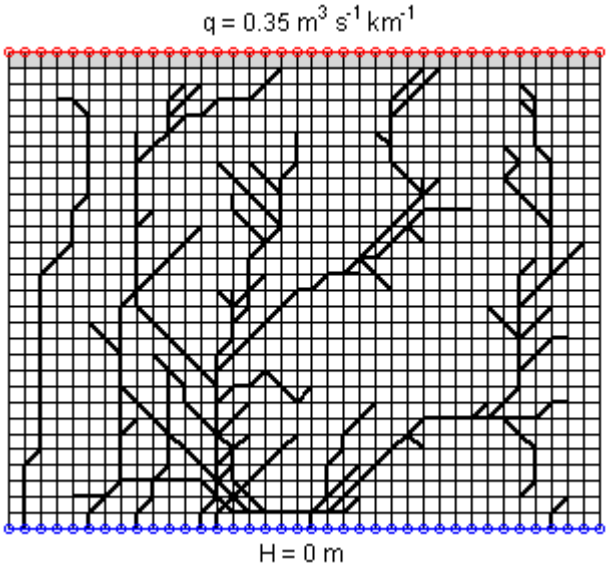

Figure 15 : Schematized view of the flow model with boundary conditions. In bold are the 1D-elements representing karstic conduits, in white, the limestone matrix elements, and in gray , matrix elements with a high hydraulic conductivity.

The groundwater flow in matrix elements is computed using Darcy's law for porous media. On the other hand, 1D elements are considered as pipes. Velocities are thus calculated with the non-linear Manning-Strickler formula for turbulent flow in pipes:

$$\boldsymbol{v = K_s \cdot \sqrt[2]{I} \cdot \sqrt[3]{R^3}} \qquad \textbf{(5)}$$

K_s, the friction coefficient, is characteristic of the pipe. A homogenous K_s of 50 is defined for the whole network. This value is proposed by Lauterjung and Schmidt (1989) for irregular concrete surfaces. I is the hydraulic gradient and R the hydraulic radius. In the model, pipes are assumed to be saturated, so the hydraulic radius is equal to the physical radius of the conduit. The identification of this parameter is described in the following paragraphs.

A constant head boundary condition is applied at the downstream border of the model in order to represent the sea. Its value is thus set to 0 meter. The upstream border is defined as an inflow boundary. Rainfalls are neglected, so it is assumed that the observed coastal outflow is directly flowing from the model upstream limit. In their review, Bauer-Gottwein et al. (2011) state that coastal outflow estimates for southern Quintana Roo range from 0.27 $m^3\ s^{-1}$ to 0.73 $m^3\ s^{-1}$ per kilometer of coastline. After comparing these values by means of numerical flow models, they suggest an outflow of 0.3 to 0.4 $m^3\ s^{-1}$ per kilometer. The upstream influx was thus set as 0.35 $m^3\ s^{-1}$ per kilometer. A row of very high conductivity elements (10^5 m s^{-1}) is added at the upstream border, so that the inflow is distributed between the matrix and the conduits (Figure 15).

The parameters that are expected to have a significant influence on the flow simulation are: 1) the matrix hydraulic conductivity, 2) the karstic network density and 3) karstic conduit diameters. In order to calibrate the model, output flow fields are compared with 43 GPS groundwater level measurements.

They were realized in cenotes and boreholes over the modeled area during February 2011 (Figure 3b). Six of those points were monitored during the 10 previous months with pressure sensors. Monitoring data reveals a tidal influence on the piezometric level in the range of 10 cm, whereas the maximum observed head is 37 cm with respect to the averaged measured sea level (6 measurements). On the other hand, the estimated measurement uncertainty is approximately 5 cm. This data are thus highly uncertain. Considering this fact, simulations were calibrated with the aim of reproducing the overall gradient, rather than with a point to point comparison. Regardless to tidal fluctuations, minimum and maximum gradients were computed by a linear regression of the punctual observed heads versus the distance to the coast. The 95% confidence interval of the gradient is 2.74 ± 0.5 cm km^{-1}. This is illustrated in Figure 13 and in Appendix C.

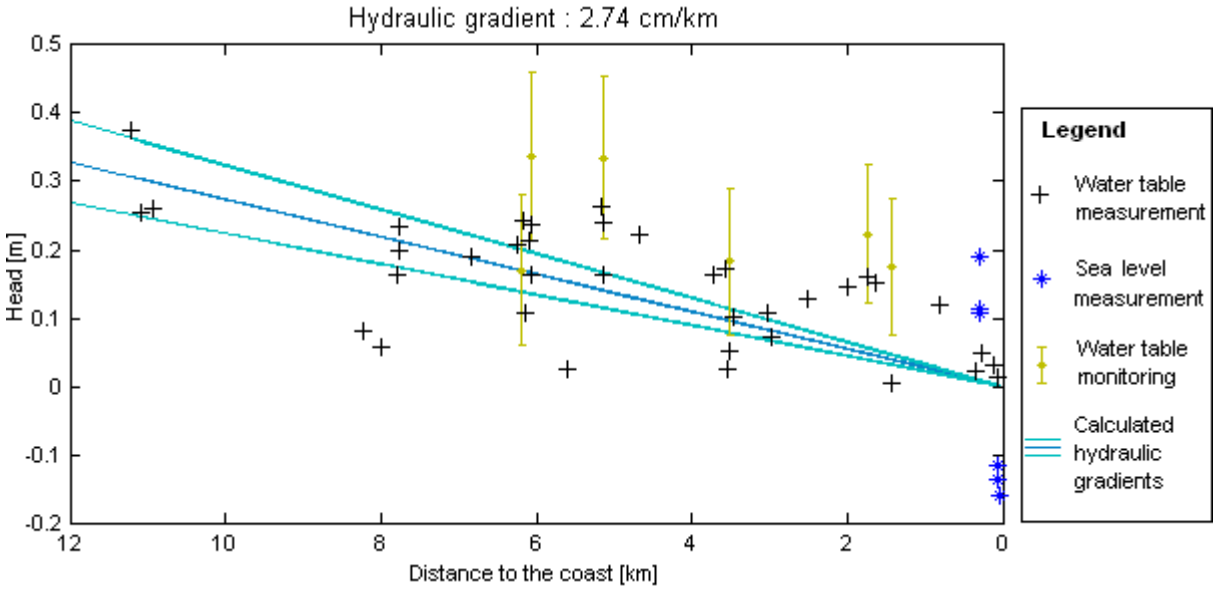

Figure 16 : Measured hydraulic heads versus distance to the coast. Measurements were taken in cenotes and boreholes in the modelized area. Six boreholes were monitored for 10 months at a rate of one measurement every 30 minutes (in gold, error bars being the standard deviation of the measurements). A hydraulic gradient of 2.24 cm km^{-1} results from the linear regression of the punctual measurements.

4.2 Sensitivity test of hydraulic parameters

To assess the influence of the matrix transmissivity T_{mat} and conduit radius r on simulated hydraulic heads, a series of simulations were run. The same karstic network is used for each simulation. As the hydraulic conductivity contrast between matrix elements and conduit element increases between each simulation, the output flow field of one simulation is used as initial conditions for the next one. The solution is thus more easily computed by the program.

Figure 17 shows the maximum simulated head for T_{mat} ranging from 10^{-6} to $10^{-1.5}$ m^2 s^{-1} and r 1 to 10 meters. It appears that T_{mat} has a smaller influence on the simulated flow field than conduit radius. Simulations that reproduce realistic hydraulic head ranges (i.e. less than 1 m) are not influenced by T_{mat} variations. It suggests that most of the flow is drained by the conduit network. For the following simulations, a transmissivity of 10^{-4} m^2 s^{-1} was selected.

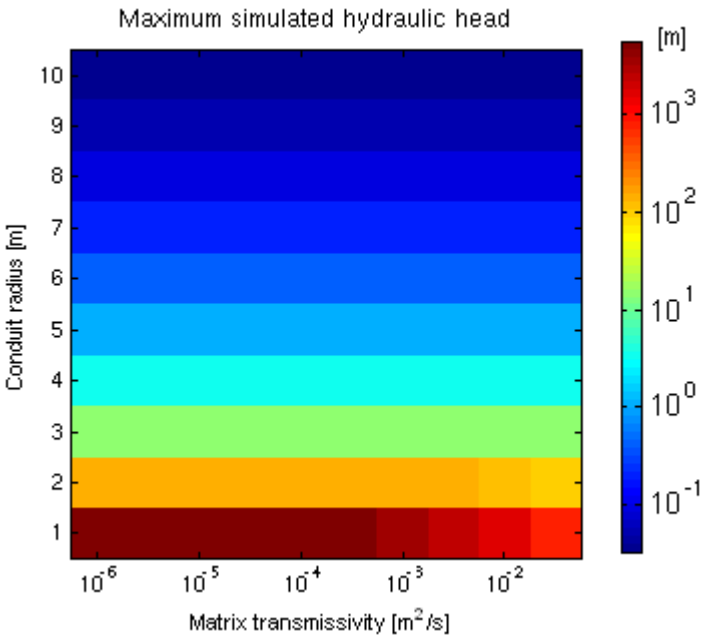

Figure 17 : Maximum simulated heads resulting from a series of simulations testing the influence of the matrix transmissivity and conduit radius.

4.3 Calibration of karst network parameters

As no measurements are available, the ordering of the network is used to assign a radius to each conduit. The karst network is regarded as an ordered river system (Figure 14) in order to apply Horton's laws (Horton, 1945). These equations have been developed to describe several features of river channels, such as drainage area, segment length and channel slope, according to their order. In this study, a generalization of Horton's laws is applied:

$$r = \alpha \cdot e^{\beta \cdot u} \qquad (6)$$

where r is the conduit radius and u the conduit order. α and β are empirical parameters that characterize the system.

A series of simulations with varying α and β for three increasing network densities (Table 1, Figure 14) were run. Both α and β range from 0.1 to 1.6. An overview of the maximum head of each simulated flow field is shown in a. It appears that α and β have an important control on the flow simulation. However, the three conduit densities yield similar results. Numerous model configurations with large conduit radius could not be solved numerically (in gray in Figure 18a). This is probably due to the high conductivity contrast between matrix elements and conduits, which prevents the solution to converge.

Based on the calculated gradient of 2.74 ± 0.5 cm km^{-1}, hydraulic heads at the upstream limit of the model (11.8 km from the coast) should lie between 26 to 38 cm (Figure 16). Simulations that yield maximum heads in this range are shown in b. They are considered to be good approximations of the system. A parameter summary of each simulation is presented in Table 2.

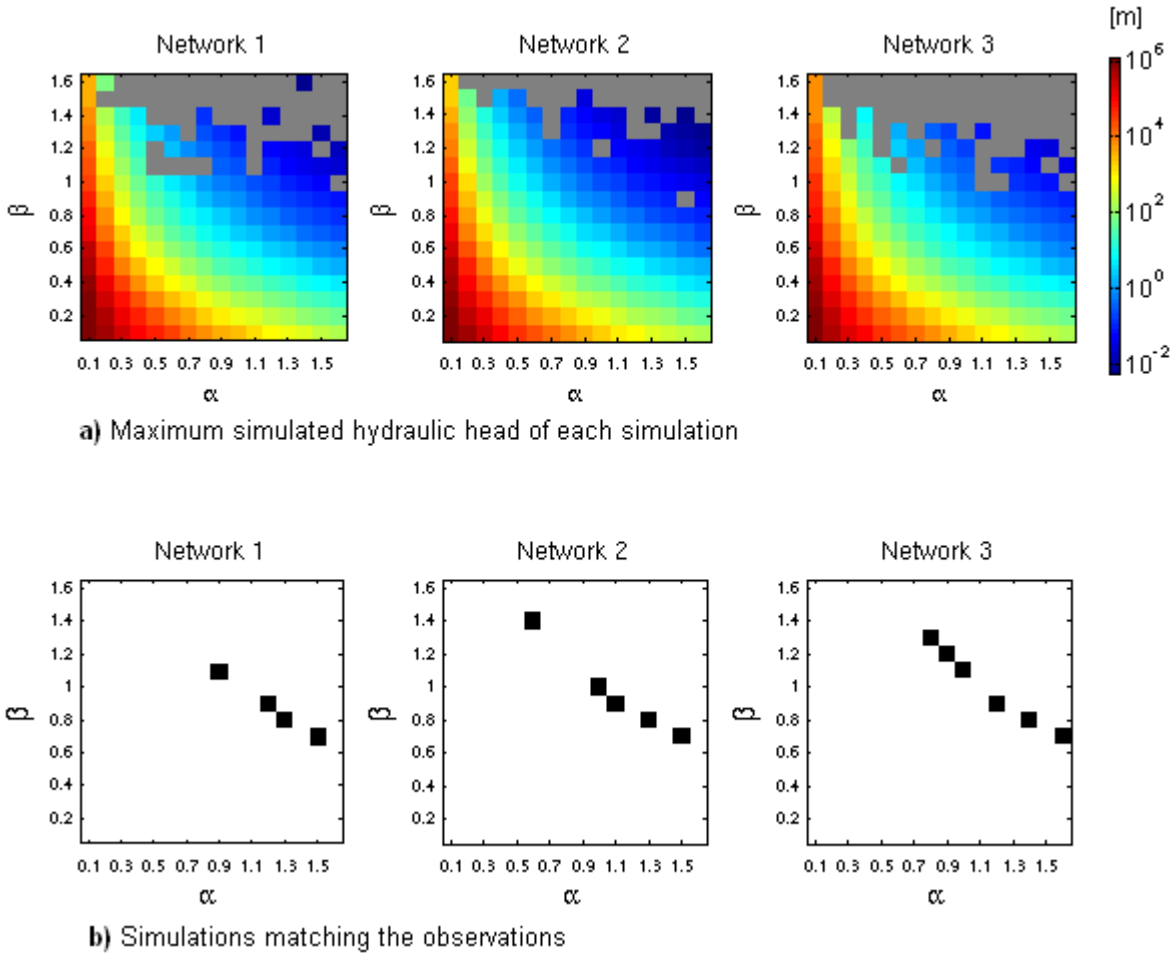

Figure 18 : a) Maximum simulated hydraulic head (in meters, on a logarithmic scale) for a set of simulations. In gray are the models for which the simulator could not compute a solution. The varying parameters are *α* and *β*, empirical parameters defining the radius of each conduit order, and the network density (increasing from network 1 to 3, see Figure 14). b) Models that yield a maximum head matching the observed gradient.

Table 2 : Parameters summary of the simulations yielding realistic hydraulic gradient (measured gradient : 2.74 ± 0.5 cm km^{-1}). Referred network densities are shown in Figure 14.

Order 1 radius [m]	Order 2 radius [m]	Order 3 radius [m]	Network density	Overall simulated gradient [cm km^{-1}]	Maximum simulated velocity [m s^{-1}]
2.7	8.1	24.4	1	3.21	0.93
3.0	7.3	17.9	1	2.37	0.78
2.9	6.4	14.3	1	3.02	0.82
3.0	6.1	12.2	1	3.02	0.75
2.4	9.9	40.0	2	2.74	0.77
2.7	7.4	20.1	2	2.29	0.71
2.7	6.7	16.4	2	2.73	0.75
2.9	6.4	14.3	2	2.35	0.68
3.0	6.1	12.2	2	2.43	0.64
2.9	10.8	39.5	3	2.69	0.85
3.0	9.9	32.9	3	2.50	0.82
3.0	9.0	27.1	3	2.50	0.81
3.0	7.3	17.9	3	3.03	0.83
3.1	6.9	15.4	3	2.57	0.74
3.2	6.5	13.1	3	2.58	0.68

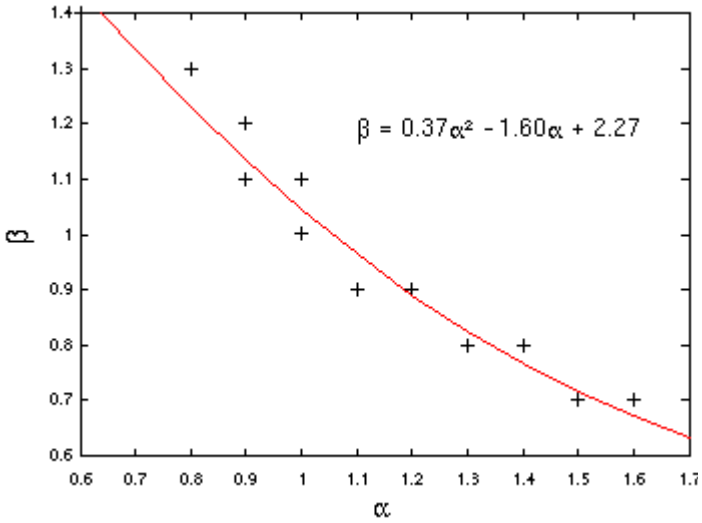

Figure 19 : Second order least-squares fit of the combinations of α and β that yield realistic flow fields.

It appears that three network densities equally provide good fits. As for the conduit radiuses, they range from 2.4 to 3.2 meters for conduit order 1, from 6.1 to 10.8 for order 2, and from 12.2 to 40.0 for order 3. It can be observed in Figure 18b that α and β satisfying combinations seem to follow a trend. This is illustrated in Figure 19. The second order least-squares fit of α versus β yield the relation

$$\boldsymbol{\beta = 0.37\,\alpha^2 - 1.60\alpha + 2.27} \qquad \textbf{(7)}$$

Maximum conduit velocities of the selected simulations are presented in Table 2. They are in the range of 1 m s^{-1}. The output flow and velocity fields of one of these simulations are shown in Figure 20. The heterogeneity of the piezometric and velocity maps confirms the strong influence of the conduits on flow simulation. Especially in the velocity map, one can observe that water flows at aprroximately 1 m y^{-1} in the matrix, while in major conduits velocities are higher than 1 cm s^{-1}. This suggest that a large majority of the flow occurs in the conduits.

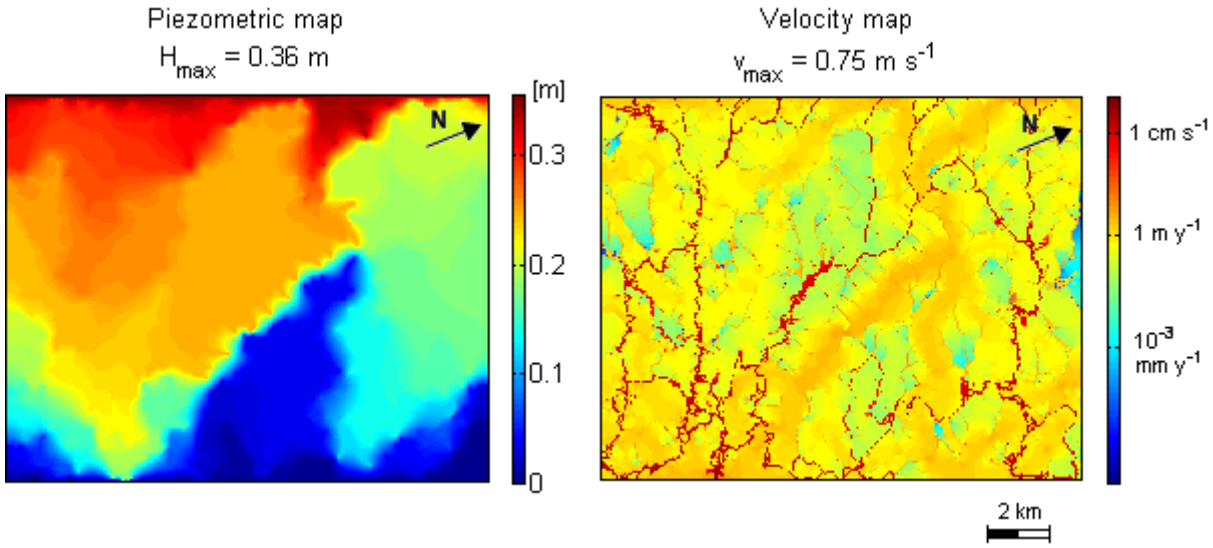

Figure 20 : Piezometric and velocity maps simulated with network 1, α = 1.5 and β = 0.7.

5. Discussion

The hydrogeological model built in this study is subject to much uncertainty. A set of 15 tested parameter configurations yield hydraulic fields that match hydraulic head observations, out of more than 700 tested models. In addition, a wide set of stochastic karst networks can be generated with the chosen input parameters. It can however be observed that the satisfying combinations of parameters α and β tend to follow a specific trend for each of the three proposed network densities.

The uncertainty of the model arises on the one hand from the lack of conditioning data and on the other hand from the karstic nature of the aquifer. The punctual water level measurements are difficult to handle, regarding the fact that the measurement accuracy is 5 cm whereas the hydraulic gradient is only a few centimeters per kilometer. In addition, tidal fluctuations observed in boreholes (~10 cm) have not been taken into account for the calculation of the hydraulic gradient. An in-depth study of the tidal wave propagation in the aquifer (delay, amplitude decay) is necessary in order to interpret more precisely piezometric levels. Finally, water table in karstic aquifers is strongly influenced by the position of conduits. Thus, a regional interpretation of punctual measurements regardless of the karst configuration lacks of relevance.

Furthermore, a high level of uncertainty is linked with the conduit radius estimates. As no measurements were available, the network was oversimplified in three radius classes. The application of an analogy of Horton laws for radius estimates is questionable as the ordering does not respect the standard Horton or Strahler ordering systems that are typically used. However, such orderings are not directly applicable to anastomosed systems. The method used in this study is quite similar, except that the confluence of numerous channels of the same order is required for the emergence of a channel of higher order.

The necessity of including highly conductive flow channels in karst aquifer models has been pointed out by many authors, for example Kiraly (1998) and Worthington (2009). This cannot go without a high uncertainty – thorough exploration of the caves is unrealistic, even in this study case where extensive cave maps were available. Furthermore, the available electromagnetic measurements constitute a major clue for the completion of the network. Their potential in revealing karstic conduits has been established in previous studies (Ottowitz, 2009; Supper et al., 2009). It has been shown in this work that they can be used successfully to constrain the simulation of stochastic karst networks.

Although the positioning of conduits is somehow uncertain, flow models presented in this work yield more realistic simulated water table and flow paths than any homogenous or distributed equivalent porous medium model. Indeed, groundwater flow is widely drained by the cave network. This is in agreement with the statement of Worthington et al. (2000) that 99.7% of the flow in this aquifer occurs in the conduits. Moreover, the simulation of turbulent flow in conduits allows realistic velocity and travel time estimates. These are essential when addressing questions of contaminant transport.

About the pollution risk, the results of flow simulations suggest that the vulnerability of the aquifer is extremely high. Indeed, computed velocities in conduits are in the order of tens of cm s^{-1}, which is unusually rapid for groundwater flow. This is in line with the *in-situ* observation of strong currents by divers, but should yet be confirmed by proper measurements. It infers that wastewater travel-times from the injection point to the outlets are short. Pollutant decay and/or absorption processes that could reduce water toxicity are thus inhibited.

Tulum wastewater is likely to travel to the sea at a very rapid rate. Indeed, cave maps indicate the presence of three explored conduits just beneath the town (Figure 3a). Based on the proposed conduit probability map (Figure 12b), it is highly probable that a straight connection exists between Tulum and the sea. According to the velocities computed by flow simulations, water could travel this 3-kilometers distance in less than one hour. This is alarming considering the major coral reef that lies near the coast. On another hand, a karstic connection between Tulum and Sian Ka'an Biosphere Reserve is not excluded. More likely, pollutions could travel from the sea to Sian Ka'an lagoons. That induces a major pollution risk for the protected ecosystems hosted in this area. To quantify this risk, better understanding of the karst network and a study of the potential contaminant sources are required.

6. Conclusions

This study presents the development of a flow model of the karstic aquifer located on the eastern coast of the Yucatan Peninsula. The karst network is intregated in the model as 1D pipes in order to simulate the turbulent flow occurring in the conduits. By use of an electromagnetic map resulting from extensive geophysical surveys, the know karst network is completed using a stochastich pseudo-genetic karst simulator. The resulting network is integrated in the model mesh.

This modeling method allows the simulation of a highly heterogeneous flow field characteristic of karstic aquifer. Realistic conduit velocities are thus estimated. Based on the simulations results, it appears that water injected nearby the town of Tulum travels very quickly to the sea. This needs to be confirmed by *in-situ* velocity measurements. This is alarming, considering the lack of wastewater treatment in this area. Further work is required to assess the potential impact of the ongoing urbanization of Tulum: better understandings of groundwater flow and of the karst network geometry, improvement of the flow model in order to realize contaminant transport simulations.

References

Bauer-Gottwein, P. et al., 2011. Review: The Yucatán Peninsula karst aquifer, Mexico. Hydrogeology Journal, 19(3): 507-524.

Beddows, P.A., 2004. Groundwater hydrology of a coastal conduit carbonate aquifer: Carribean coast of the Yucatán Peninsula, México. PhD Thesis, University of Bristol, Bristol, 303 pp.

Beddows, P.A., Smart, P.L., Whitaker, F.F. and Smith, S.L., 2007. Decoupled fresh-saline groundwater circulation of a coastal carbonate aquifer: Spatial patterns of temperature and specific electrical conductivity. Journal of Hydrology, 346(1-2): 18-32.

Borghi, A., Renard, P. and Jenni, S., 2011. A pseudo-genetic stochastic model to generate karstic networks. Journal of Hydrology, under review.

Cooper, H.H., 1959. A hypothesis concerning the dynamic balance of fresh water and salt water in a coastal aquifer. Journal of Geophysical Research, 64(4): 461-467.

Cornaton, F., 2007. Ground Water : A 3-D Ground Water and Surface Water Flow, Mass Transport and Heat Transfer Finite Element Simulator, Reference Manual. University of Neuchâtel (Switzerland), 418 pp.

Gondwe, B.R.N., 2010. Exploration, modelling and management of groundwater-dependent ecosystems in karst – the Sian Ka'an case study, Yucatan, Mexico. PhD Thesis, Technical University of Denmark, Kongens Lyngby, 86 pp.

Gondwe, B.R.N. et al., 2010. Hydrogeology of the south-eastern Yucatan Peninsula: New insights from water level measurements, geochemistry, geophysics and remote sensing. Journal of Hydrology, 389(1-2): 1-17.

Héraud-Piña, M.-A., 1996. Le Karst du Yucatan, Pays des Mayas. Presses Universitaires de Bordeaux, Bordeaux, 284 pp.

Horton, R.E., 1945. Erosional development of streams and their drainage basins - Hydrophysical approach to quantitative morphology. Geological Society of America Bulletin, 56(3): 275-370.

Huang, H., 2008. Airborne geophysical data leveling based on line-to-line correlations. Geophysics, 73(3): F83-F89.

Iturralde-Vinent, M.A. and MacPhee, R.D.E., 1999. Paleogeography of the Caribbean region: Implications for cenozoic biogeography. Bulletin of the American Museum of Natural History(238): 1-95.

Kiraly, L., 1998. Modelling karst aquifers by the combined discrete channel and continuum approach. Bulletin du Centre Hydrogéologie de Neuchâtel, 16: 77-98.

Lauterjung, H. and Schmidt, G., 1989. Planning of Water intake structures for irrigation or hydropower, Planning for intake structures. Deutsche Gesellschaft für Technische Zusammenarbeit (GTZ) GmbH.

Mariethoz, G., Renard, P. and Straubhaar, J., 2010. The Direct Sampling method to perform multiple-point geostatistical simulations. Water Resour. Res., 46(11): W11536.

Marin, L., Steinich, B., Pacheco, J. and Escolero, O., 2000. Hydrogeology of a contaminated soil-source karst aquifer, Mérida, Yucatán, Mexico. Geofísica Internacional, 39(004): 359-365.

Moore, Y.H., Stoessell, R.K. and Easley, D.H., 1992. Fresh-water sea-water relationship within a groundwater-flow system, northeastern coast of the Yucatan Peninsula. Ground Water, 30(3): 343-350.

Motschka, K., 2001. Aerogeophysics in Austria. Bulletin of the Geological Survey of Japan, 52(2/3): 83-88.

Ottowitz, D., 2009. 3D-Modellrechnung der Karststrukturen des Ox Bel Ha Höhlensystems zur Methodenevaluierung – Aeroelektromagnetik. MSc Thesis, University of Vienna, Vienna, 123 pp.

SCT, 2010. Manifestación de Impacto Ambiental Modalidad Regional Construcción del Libramiento de Tulum, en el Estado de Quintana Roo, Secretaría de Comunicaciones y Transportes, México.

SGM, 2007. Carta geológico-minera : Estado de Campeche, Quintana Roo y Yucatán. Servicio Geológico Mexicano.

Smart, P.L. et al., 2006. Cave development on the Caribbean coast of the Yucatan Peninsula, Quintana Roo, Mexico. In: R.S. Harmon and C.M. Wicks (Editors), Perspectives on Karst Geomorphology, Hydrology, and Geochemistry - a Tribute Volume to Derek C. Ford and William B. White. Geological Society of America Special Papers. Geological Soc Amer Inc, Boulder, pp. 105-128.

Stoessell, R.K., Coke, J.G. and Easley, D.H., 2002. Localized thermal anomalies in haloclines of coastal Yucatan sinkholes. Ground Water, 40(4): 416-424.

Supper, R. et al., 2009. Spatial mapping of submerged cave systems by means of airborne electromagnetics: an emerging technology to support protection of endangered karst aquifers. Near Surface Geophysics, 7(5-6): 613-627.

Thomas, C., 2010. Le karst du Yucatàn: rôle du flux géothermique, des failles, de l´eau de mer et des évaporites dans sa genèse. Karstologia, 55: 1-18.

Vacher, H.L. and Mylroie, J.E., 2002. Eogenetic karst from the perspective of an equivalent porous medium. Carbonates and Evaporites, 17(2): 182-196.

Ward, W.C., Keller, G., Stinnesbeck, W. and Adatte, T., 1995. Yucatan subsurface stratigraphy: Implications and constraints for the Chicxulub impact. Geology, 23(10): 873-876.

Worthington, S.R.H., Ford, D.C. and Beddows, P.A., 2000. Porosity and permeability enhancement in unconfined carbonate aquifers as a result of solution. In: A. Klimchouk, Ford, D.C., Palmer, A.N. and Dreybrodt, W. (Editor), Speleogenesis: Evolution of karst aquifers, Huntsville, pp. 463-472.

Worthington, S.R.H. and Smart, C.C., 2003. Groundwater in karst: mathematical models. In: J. Gunn (Editor), Encyclopaedia of Caves and Karst., pp. 401-403.

Worthington, S.R.H., 2009. Diagnostic hydrogeologic characteristics of a karst aquifer (Kentucky, USA). Hydrogeology Journal, 17(7): 1665-1678.

Appendix A : Measured electromagnetic response

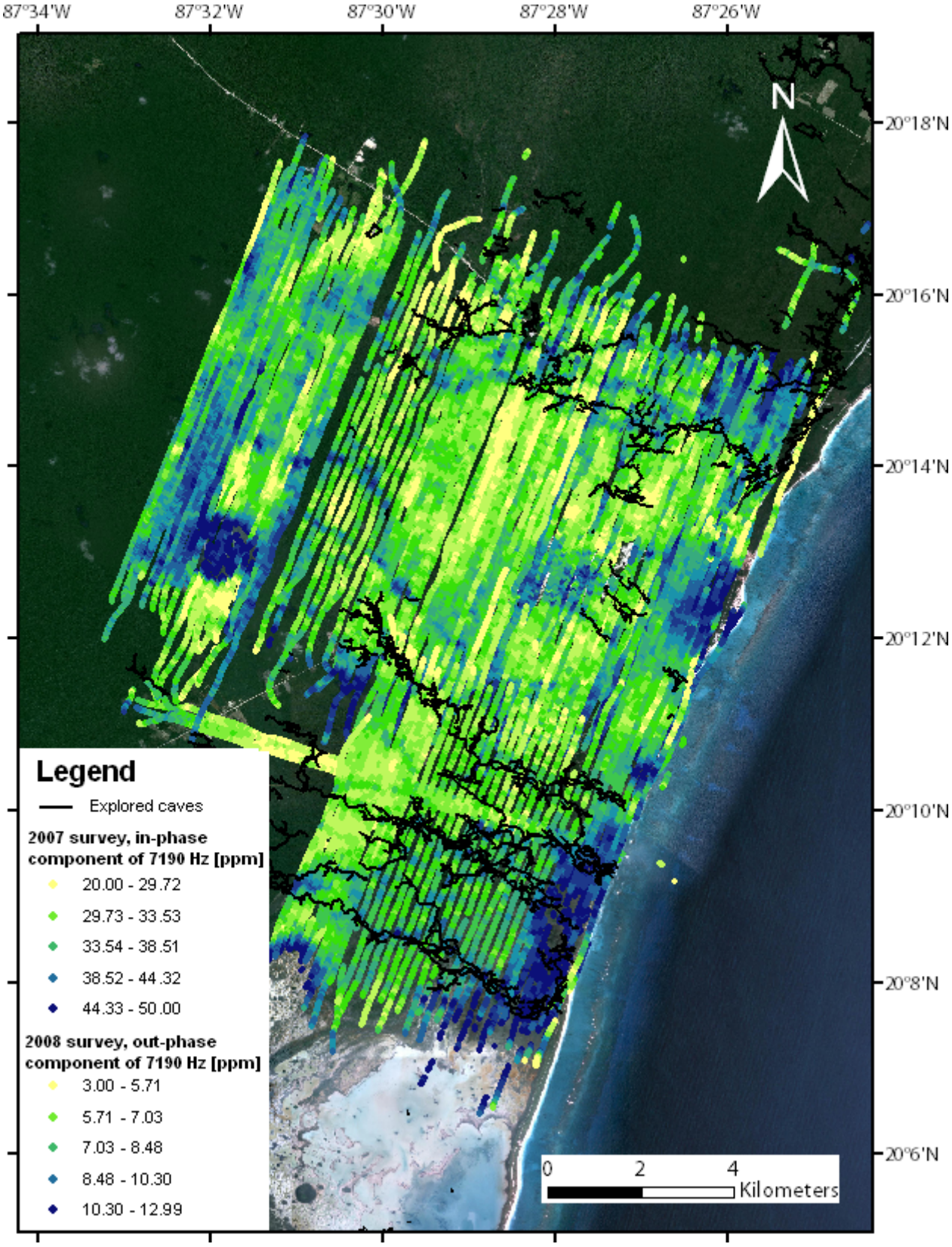
87°34'W
87°32'W
87°30'W
87°28'W
87°26'W
20°18'N
20°16'N
20°14'N
20°12'N
20°10'N
20°8'N
20°6'N
N
Legend
Explored caves
2007 survey, in-phase component of 7190 Hz [ppm]
20.00 - 29.72
29.73 - 33.53
33.54 - 38.51
38.52 - 44.32
44.33 - 50.00
2008 survey, out-phase component of 7190 Hz [ppm]
3.00 - 5.71
5.71 - 7.03
7.03 - 8.48
8.48 - 10.30
10.30 - 12.99
0
2
4
Kilometers

Appendix B : Processed electromagnetic response

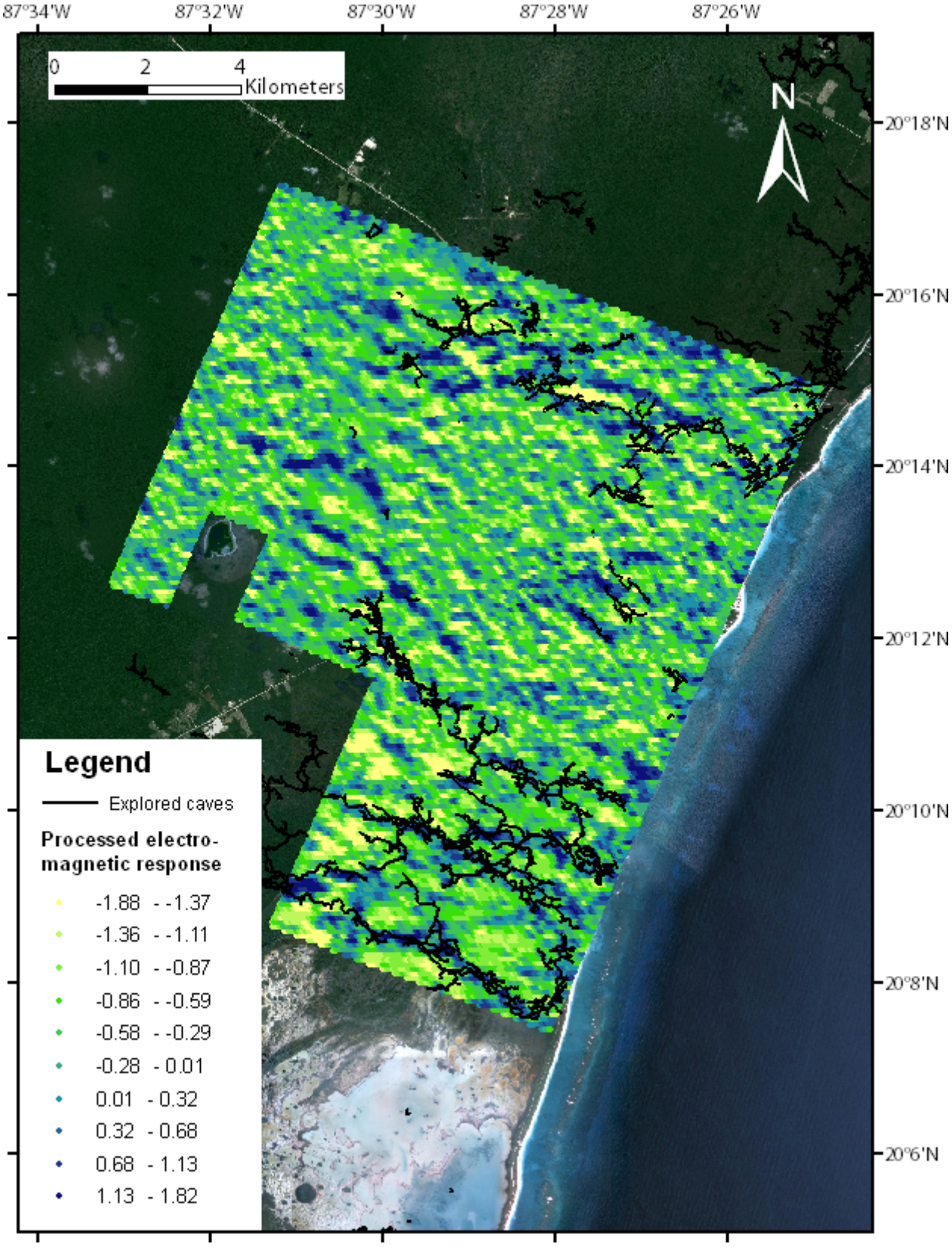
87°34'W
87°32'W
87°30'W
87°28'W
87°26'W
20°18'N
20°16'N
20°14'N
20°12'N
20°10'N
20°8'N
20°6'N
0
2
4
Kilometers
N
Legend
Explored caves
Processed electro-magnetic response
-1.88 - -1.37
-1.36 - -1.11
-1.10 - -0.87
-0.86 - -0.59
-0.58 - -0.29
-0.28 - 0.01
0.01 - 0.32
0.32 - 0.68
0.68 - 1.13
1.13 - 1.82

Appendix C : Water level measurements

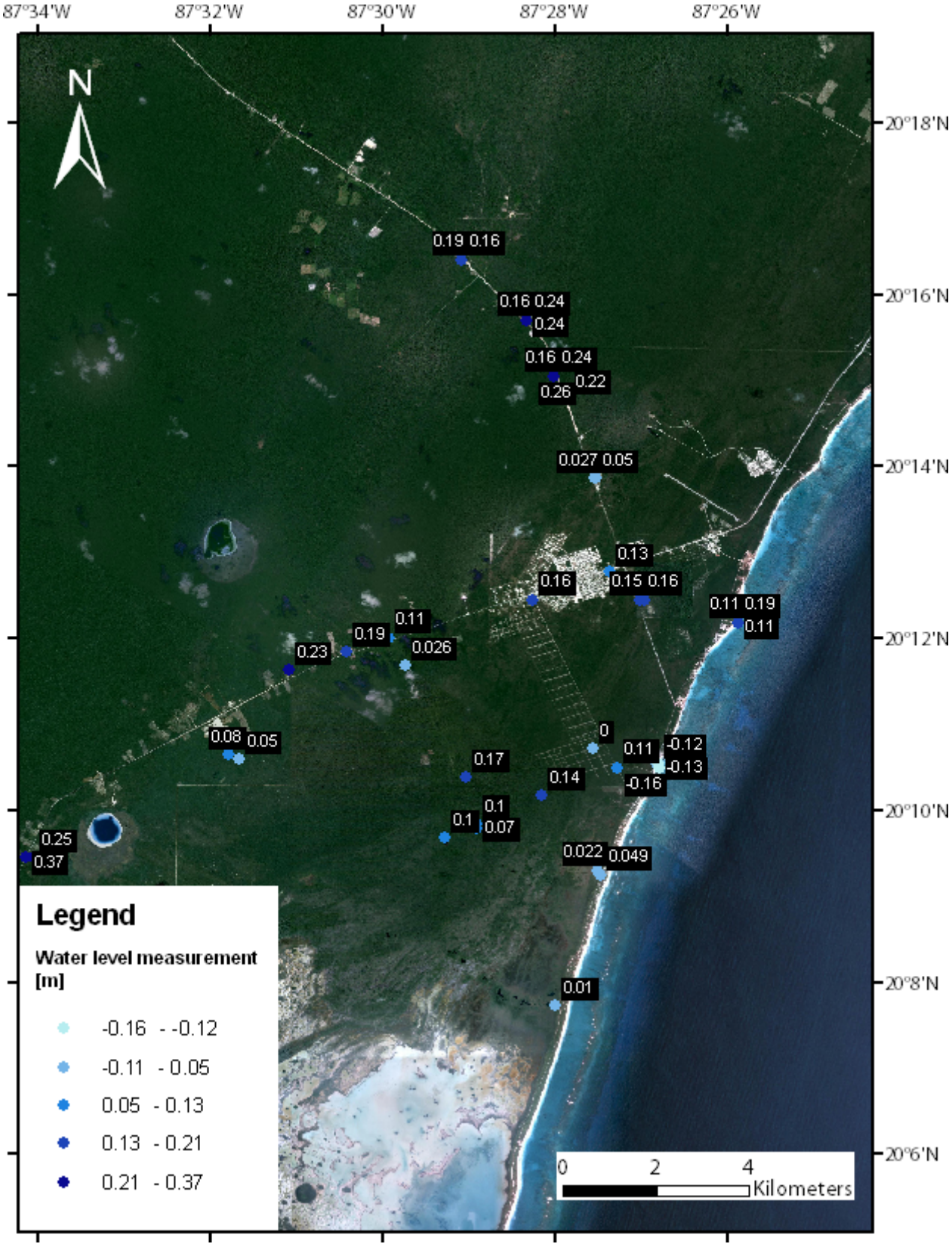
87°34'W
87°32'W
87°30'W
87°28'W
87°26'W
20°18'N
20°16'N
20°14'N
20°12'N
20°10'N
20°8'N
20°6'N
N
0.19 0.16
0.16 0.24
0.24
0.16 0.24
0.22
0.26
0.027 0.05
0.13
0.16
0.15 0.16
0.11 0.19
0.11
0.11
0.19
0.23
0.026
0.08 0.05
0
0.11
-0.12
-0.13
-0.16
0.17
0.14
0.1
0.1
0.07
0.25
0.37
0.022 0.049
0.01
Legend
Water level measurement [m]
-0.16 - -0.12
-0.11 - 0.05
0.05 - 0.13
0.13 - 0.21
0.21 - 0.37
0
2
4
Kilometers